



# Effects of a single spanwise surface wire on a free-ended circular cylinder undergoing vortex-induced vibration in the lower synchronization range

E. Vaziri<sup>1</sup> and A. Ekmekci<sup>1,†</sup>

<sup>1</sup>University of Toronto Institute for Aerospace Studies, Toronto, ON M3H 5T6, Canada

(Received 13 October 2021; revised 29 August 2022; accepted 9 September 2022)

This experimental study investigated the control induced by a spanwise surface wire on a rigid circular cylinder undergoing vortex-induced vibration (VIV) under the conditions of low mass damping in the lower synchronization branch. Being motivated by the idea of VIV-based energy harvesting from ocean and river flows, this elastically mounted cylinder was immersed in a water channel, leaving a free end at its bottom spanwise end, while the free water surface bounded its top. The cylinder was constrained to vibrate in the cross-stream direction. The wire diameter was 6.25 % of the cylinder diameter. Experimental research was conducted by attaching this large-scale wire along the span of the cylinder at various angular positions ranging from 0° to 180° (with respect to the most upstream point of the cylinder) at a fixed Reynolds number of 10<sup>4</sup> (based on the cylinder diameter). Simultaneous to measuring the trajectory of the cylinder motion via a laser distance sensor, the instantaneous velocity field in the near wake of the cylinder was obtained using particle image velocimetry. Several VIV response categories were identified depending on the angular position of the wire, which led to the classification of distinct angular ranges for the wire application. Associated with the structural vibrations in these categories, different vortex-formation modes induced by the wire were revealed. For specific wire positions, decreases of up to 98 % and increases of up to 102 % were identified in the oscillation amplitude of the cylinder compared with the amplitude of the clean cylinder under similar conditions.

**Key words:** flow-structure interactions, vortex shedding, flow control

† Email address for correspondence: [alis.ekmekci@utoronto.ca](mailto:alis.ekmekci@utoronto.ca)

© The Author(s), 2022. Published by Cambridge University Press. This is an Open Access article, distributed under the terms of the Creative Commons Attribution-NonCommercial-NoDerivatives licence (<http://creativecommons.org/licenses/by-nc-nd/4.0>), which permits non-commercial re-use, distribution, and reproduction in any medium, provided that no alterations are made and the original article is properly cited. The written permission of Cambridge University Press must be obtained prior to any commercial use and/or adaptation of the article.

## 1. Introduction

Vortex-induced vibration (VIV) is a significant phenomenon affecting many engineering structures in fluid flow. These structures can be, for example, offshore risers used in petroleum extraction, heat exchanger tubes in nuclear plants, aircraft control surfaces in aeronautical applications and civil engineering structures such as bridges, towers and industrial chimneys, to name a few. The cause of VIV is the periodic vortex shedding from an elastic or elastically mounted rigid bluff structure. Periodically shed vortices impose alternating pressure forces on the surface of the structure, and these forces can lead to large-amplitude structural vibrations if the vortex shedding frequency is close to the natural frequency of the structure. The present knowledge base researchers have developed on the VIV of cylinders over the years is discussed in detail in the reviews of Sarpkaya (2004), Williamson & Govardhan (2004, 2008), Gabbai & Benaroya (2005), Nakamura & Kaneko (2008) and Naudascher & Rockwell (2012).

The VIV of an elastically mounted rigid cylinder in the transverse direction mainly depends on the mass ratio ( $m^* = m_t/m_d$ ), damping ratio ( $\zeta = c_{sys}/c_{crit}$ ) and reduced velocity ( $U^* = U/f_n D$ ), where  $m_t$  is the total mass of the oscillating system,  $m_d$  is the mass of the displaced fluid,  $c_{sys}$  is the damping of the system,  $c_{crit}$  is the critical damping,  $U$  is the free-stream velocity,  $f_n$  is the natural frequency of the system and  $D$  is the cylinder diameter. The dependency of the transverse VIV response on these parameters has been experimentally investigated by many studies, such as Khalak & Williamson (1997a). For an elastically mounted cylinder with a high mass-damping parameter,  $m^*\zeta$ , the work of Feng (1968) showed that the amplitude of transverse-direction VIVs in the synchronization range follows two response branches as the reduced velocity is varied: commonly named as the initial branch and the lower branch. On the other hand, for a system with a low mass-damping parameter, Khalak & Williamson (1997b) showed that three response branches exist: namely, initial, upper and lower branches. It should be noted that some studies, such as Sarpkaya (2004), consider the added mass coefficient  $C_a$  in the calculation of the mass-damping parameter, which then takes the form of  $(m^* + C_a)\zeta$  rather than  $m^*\zeta$ . The added mass is related to the coupling of the cylinder motion to the surrounding fluid and is equal to the mass of fluid displaced by the volume of the immersed structure multiplied by an added mass coefficient  $C_a$ . For a circular cylinder in unconfined flow, the added mass coefficient takes the value of  $C_a = 1$ .

A further parameter that affects the free vibration response of a cylinder in the transverse direction is identified to be its spanwise end condition by Morse, Govardhan & Williamson (2008). They conducted their tests in a water tunnel under low mass-damping conditions. The top end of their submerged cylinder was bounded by the free surface of the water, while for the bottom end, the following three end conditions were tested: a plate unattached from the cylinder, a plate attached to the cylinder and a free end with no endplate. They saw that the free vibration response, with its well-documented initial, upper and lower branches, is virtually the same for the attached and unattached plate cases, provided that the unattached plate is sufficiently close to the cylinder's end. On the other hand, without an endplate, they found that the vibration amplitudes in the lower branch increase significantly, and the transitional jump between the upper and lower branches disappears. Also, although the maximum amplitude in the upper branch remains unchanged for the no endplate case compared with the case with an endplate, the time traces of the cylinder displacement with no endplate differ from their characteristic patterns found under the effect of an endplate for both the upper and lower branches. Perhaps the most remarkable finding of their study is that the vibration response of a cylinder with an unattached endplate becomes equivalent to having no plate at all when the unattached plate is placed

at a sufficient distance away from the cylinder. This distance was argued to be around 15 % of the cylinder diameter and higher, which for a 50.8 mm cylinder corresponds to a distance of nearly 7 mm and above.

Brika & Laneville (1993) were the first to show a correspondence between the vortex shedding patterns and the response branches in the synchronization regime. In their wind tunnel tests of a high mass-damping flexible cable that is allowed to undergo transversal free vibrations, they found that the initial and lower response branches, which are the only two response branches encountered in a system with a high mass-damping parameter, are associated with the vortex shedding patterns, denoted as 2S and 2P modes, respectively. The naming of these modes follows the terminology used by Williamson & Roshko (1988) for the vortex patterns of forced oscillating cylinders. In the 2S mode, two single vortices are shed per cycle, and vortices travel downstream along the centreline of the oscillating cylinder. In the 2P mode, two vortex pairs are shed per cycle, and they travel laterally outward from the wake centreline while convecting downstream. Govardhan & Williamson (2000) showed for the first time that the 2P mode of vortex formation also exists in the upper branch, which is the additional high-amplitude response branch encountered in systems with low mass-damping. Subsequently, Morse & Williamson (2009) discovered, in their study, a new vortex mode for the upper branch and called it the 2P<sub>0</sub> mode. In the 2P<sub>0</sub> mode, two vortex pairs are formed in each cycle, similar to the 2P mode, but the second vortex in each pair is much weaker than the first vortex. Furthermore, they demonstrated that the 2S, 2P and 2P<sub>0</sub> modes result in positive excitation from vortex-induced forces, which is a necessary condition for free structural vibrations to occur, and among these modes, the 2P<sub>0</sub> mode yields the peak resonant amplitude within the synchronization region.

While analysing the vibration response and the associated vortex modes, as discussed by Konstantinidis (2014), the condition of lock-in (also known as synchronization) is important. In general, the lock-in condition is defined as the situation when the ratio of two frequencies is constant while some input parameter is varied. In the case of the freely oscillating cylinder, there are three characteristic frequencies: the natural frequency of the system ( $f_n$ ) determined by its mechanical properties, the frequency of the structural oscillation motion ( $f_d$ ) and the frequency of vortex shedding, which is equivalent to the frequency of streamwise and transverse flow velocity fluctuations in the wake ( $f_u$  and  $f_v$ ). Traditionally, the lock-in or synchronization during free vibrations was considered to happen when the frequency of structural oscillation, as well as the vortex shedding frequency, matches the natural frequency of the structure so that  $f_d^* = f_d/f_n \approx 1$ . This is indeed found to be true for systems with high mass ratios (Govardhan & Williamson 2000). However, for low mass ratios, a structure can oscillate at frequencies higher than its natural frequency during lock-in (for example,  $f_d^* \approx 1.4$  was reported in Khalak & Williamson 1997b). Thereby, lock-in can be defined better as the matching between the frequency of vortex shedding in the wake and the frequency of structural oscillations (Williamson & Govardhan 2004).

Several methods have been proposed and investigated so far for controlling the oscillation of structures undergoing VIV. The VIV in civil engineering structures can be avoided by altering the structures' stiffness or using vibration dampers; however, these methods are expensive and sometimes impractical compared with fluid mechanics methods that mainly modify the flow around the structure. Fluid mechanics methods of VIV control are based on energizing the boundary layer or altering the vortex shedding process. These methods include using roughness elements (Chang, Ajith Kumar & Bernitsas 2011), surface bumps (Owen, Bearman & Szewczyk 2001), splitter plates (Assi, Bearman & Kitney 2009), vortex generators (Ünal & Atlar 2010), helical strakes

(Zhou *et al.* 2011), cactus inspired spines (Levy & Liu 2013), fins (Khashehchi *et al.* 2014), dimples (Zhou *et al.* 2015), rectangular grooves (Canpolat & Sahin 2017), strips (Vinod, Auvil & Banerjee 2018), plasma actuators (Castro Hebrero *et al.* 2020) and surface wires (Hover, Tvedt & Triantafyllou 2001). The fluid mechanics methods can be employed to intensify VIV as well as to suppress it. For instance, Chang *et al.* (2011) utilized surface roughness strips to enhance VIV with the purpose of harnessing electricity from the hydrokinetic energy of ocean/river currents. By appropriately selecting the placement angle, coverage area and height of the roughness strips, they could amplify the oscillation amplitude by 1.7 times that of the clean cylinder. In contrast, Owen *et al.* (2001) used an arrangement of surface bumps to lessen VIV by suppressing vortex shedding. In their results, regular vortex shedding could not be detected for a stationary cylinder with surface bumps; however, when the same cylinder was flexibly mounted, the transverse oscillation was detectable at low values of the mass-damping parameter  $m^*\zeta$  with a maximum amplitude 25 % lower than that of the clean cylinder.

The simplest fluid mechanics control devices that can be applied on the surface of a cylindrical body are spanwise wires. Their effects on the flow and loading characteristics have been widely investigated in the literature for fixed cylinders in the subcritical flow regime. In particular, the work of Nebres & Batill (1993) has laid the groundwork for research in this area. For a stationary cylinder fitted with a single spanwise surface wire, they discussed the variation of the non-dimensionalized vortex shedding frequency with the wire diameter ( $d$ )-to-cylinder diameter ( $D$ ) ratio, wire angular position  $\theta$  and Reynolds number. They showed that the dimensionless form of the vortex shedding frequency (Strouhal number,  $St$ ) undergoes fundamental changes at multiple wire locations for a given wire diameter-to-cylinder diameter ( $d/D$ ) ratio and Reynolds number. Based on these changes, they defined several fundamental angles for a single-wire application on the cylinder surface. By carrying out particle image velocimetry (PIV) measurements, Ekmekci (2006) and Ekmekci & Rockwell (2010) examined the near-wake and shear-layer flow patterns of a stationary cylinder tripped with a single spanwise wire for various wire positions. Their results, collected at the subcritical Reynolds number of  $Re = 10^4$ , demonstrated that a single spanwise surface wire can significantly attenuate the Kármán vortex shedding from a fixed cylinder when it is placed at a specific small range of angular positions on the cylinder surface, which they called the first critical wire locations  $\theta_{c1}$ . Furthermore, they showed that the same wire can be used to intensify the Kármán vortex shedding when placed at another range of critical locations, named the second critical locations  $\theta_{c2}$ . Other than the attenuation and enhancement of the Kármán instability, they associated these two critical wire locations,  $\theta_{c1}$  and  $\theta_{c2}$ , with further distinctive characteristics. Namely, a spanwise surface wire at the first critical angle  $\theta_{c1}$  also led to a bistable flow regime, early onset of shear-layer instability in the shear layer separating from the wire side of the cylinder and significant extension in the streamwise length of the time-averaged recirculation bubble in the near wake. The same surface wire, when placed at the second critical angle  $\theta_{c2}$ , depicted increased amplitudes of shear-layer flapping, early onset of shear-layer instability and the utmost level of near-wake contraction. The subsequent work conducted by Ekmekci & Rockwell (2011) proved that only a spanwise surface wire that is larger than the boundary layer thickness can attenuate or intensify the Kármán instability at the critical locations, while a surface wire that is smaller than the boundary layer thickness was found to have no detectable impact on the strength and coherence of the Kármán vortex shedding. Soon after, Aydin, Joshi & Ekmekci (2014) confirmed that a single spanwise surface wire stops the regular formation of Kármán vortices over long periods of time when placed at a first critical wire location

$\theta_{c1}$ , but the regular shedding still resumes intermittently for short times. As a result, in the time-averaged sense, a drastic attenuation is observed in the autospectral density of velocity fluctuations at the frequency of Kármán vortex shedding. Also, Aydin *et al.* (2014) investigated the dependence of the critical wire locations on the wire size and Reynolds number (within the subcritical Reynolds number range of  $Re = 5 \times 10^3$  to  $3 \times 10^4$ ). Their results indicated that the range of  $\theta_{c2}$  is generally independent of both the Reynolds number and wire size, while the range of  $\theta_{c1}$  depends on the wire size, and for a given wire size,  $\theta_{c1}$  increases with increasing Reynolds number until the Reynolds number of  $Re = 10^4$  is reached, beyond which  $\theta_{c1}$  becomes independent of the Reynolds number within the  $Re$  range that they studied. Ekmekci (2006) and Ekmekci & Rockwell (2010) showed that the bistable phenomenon, observed when the spanwise wire is at the  $\theta_{c1}$  location, involves intermittent switching of the shear layer between the states of reattachment and no reattachment after separation from the wire. This switch in separation mode occurred at a broad, low-frequency band that is one order of magnitude smaller than the nominal Kármán vortex shedding frequency. A further independent study conducted by Alam *et al.* (2010) observed this bistable phenomenon for the case of a fixed cylinder involving two spanwise wires that are symmetrically placed with respect to the approach flow, and Joshi & Ekmekci (2019) also detected the bistable state for asymmetrically arranged spanwise surface wires when one of the wires passes from the critical location on the cylinder surface.

Spanwise surface wires can be used as a method to modify the VIV of cylinders, but few studies have been conducted on this topic. One of the earliest studies on the use of spanwise surface wires on cylinders undergoing VIV is the work of Price (1956), which involved water channel tests at a Reynolds number of  $Re = 4.64 \times 10^3$  for a cylinder fitted with three straight wires placed at the specific angles  $0^\circ$ ,  $+60^\circ$  and  $-60^\circ$  from the forward stagnation point of the cylinder. For this tripped cylinder arrangement, Price (1956) detected the same amplitude of vibration found for the clean cylinder and presumed that the spanwise surface wires are ineffective in suppressing large-scale VIV. However, the observed results were due to the wire size. The wires they used were smaller than the boundary layer thickness, and as a result, they did not influence the flow field appreciably in that work. Hover *et al.* (2001) studied the vortex-induced load and vibration characteristics at  $Re = 3.0 \times 10^4$  for a cylinder fitted with two spanwise wires (having a wire-to-cylinder diameter ratio of  $d/D = 0.3\%$ ) at the angular positions of  $+70^\circ$  and  $-70^\circ$ . These surface wires decreased the peak oscillation amplitude moderately in the reduced velocity range of  $U^* = 5.1$ – $6$ ; while above  $U^* = 6$ , the decrease in vibrations was quite substantial. In particular, at higher reduced velocities, near  $U^* = 8$  and above, their results suggest total disruption of synchronization with the addition of the wires at the particular wire position that they tested for the cylinder, which would otherwise undergo VIV in the lower synchronization branch. At such high reduced frequencies, the wires induced very-high-frequency and uncorrelated fluctuating lift and drag forces on the cylinder. More recently, the fluid forces and vibration response of an elastically mounted cylinder with two symmetrically positioned spanwise wires ( $d/D = 12\%$ ) were investigated by Quadrante & Nishi (2014) for a range of Reynolds numbers from  $3.45 \times 10^3$  to  $2.04 \times 10^4$ . They considered four angular positions for the application of the wires, and reported that the cylinder vibration is intensified when the wires are at  $\mp 60^\circ$  and  $\mp 75^\circ$  and considerably suppressed for wires at  $\mp 105^\circ$  and  $\mp 120^\circ$ . It should be noted that, in their set-up, the cylinder and the spanwise wires had a gap, which was 10% of the cylinder diameter, and their mass ratio was quite high ( $m^* = 6.13$ ).

As seen from the review of the previous studies above, while the effects of spanwise wires have been well documented for fixed cylinders, such efforts have remained very

limited for cylinders undergoing VIV. As reviewed above, only a few studies have investigated the VIV of cylinders tripped by spanwise wires, where the efforts have remained limited to having two to four wires at less than a handful of wire placement angles (at the most) on the cylinder surface, and these studies have lacked an understanding of the wire-induced changes in the flow patterns. Thus, there is an apparent lack of knowledge regarding the wire-induced flow structure and vibration response of flexibly mounted cylinders, where a wide range of wire locations needs to be systematically assessed. Furthermore, as the plurality of wires may complicate the development of a thorough understanding in the early stages, rather than starting with exploring the effects of two or more wires, as has been done in the previous VIV investigations that involved tripped cylinders, keeping the arrangement deliberately simple in the first steps by considering a single-wire application on the cylinder surface may provide guidance and explanation in deciphering the effects of more complex surface modifications. Previously, Joshi & Ekmekci (2019) used such an approach for stationary cylinders and successfully explained the origins of more complex effects of multi-wire spanwise tripping based on the understandings of single-wire tripping.

A further relevant point that has been totally overlooked by previous researchers is the effects of tripping when the cylinder undergoing VIV is free ended. All previous experiments in the literature concerning the VIV of a tripped cylinder utilized endplates that are either attached to the spanwise end of the cylinder or unattached with a very small gap from the cylinder, whereby VIV of surface-wire-fitted cylinders with a free-end condition remained unexplored. For example, Quadrante & Nishi (2014) had attached endplates at the spanwise ends of the tripped cylinder, and the endplates used in Hover *et al.* (2001) had a small gap (2.6 % of the cylinder diameter), producing a VIV response as if the endplates were attached to the cylinder in accord with Morse *et al.* (2008). As mentioned above, it is known for a plain cylinder undergoing VIV that the presence of a free spanwise end significantly changes the character of the vibration response (Morse *et al.* 2008). Understanding the effects of spanwise wires for such free-ended cylinders can find uses, for example, in energy harvesting applications. Although large-amplitude VIV in engineering structures is usually unwanted and should be avoided or mitigated to prevent structural damages, with recent advances in piezoelectric technology, VIV-based energy harvesting has started to gain attention (Erturk & Inman 2011). A recent example of such a study is the work of Azadeh-Ranjbar, Elvin & Andreopoulos (2018), where the focus was on harvesting energy from the VIV of a plain, finite-length cylinder with spanwise free ends in a wind tunnel, where the cylinder was elastically mounted on a cantilever beam equipped with a piezoelectric patch. A simple possible arrangement for a VIV-based energy harvester extracting hydrokinetic energy from ocean or river flows may involve a flexibly mounted cylinder submerged in water with its top end piercing the free surface of the water while its bottom end is essentially free. Evaluating surface wire-induced effects on the VIV response of such a system is part of the stimulus of the present paper. Enhancing the amplitude of the structural oscillations by the effect of a wire could directly maximize the harvested energy.

Taking the unresolved issues mentioned above into consideration, the current experimental research focuses on the effects of a single spanwise surface wire on the oscillation response and flow structure of a low mass-damping rigid circular cylinder undergoing VIV in the transverse direction. This elastically mounted cylinder was immersed in a free-surface water channel, leaving a free end at the bottom while its top end pierced the free surface of the water channel. To ensure that the system responds as if its bottom end is free, a sufficient gap was left between the bottom end of the cylinder

and an unattached plate in accordance with Morse *et al.* (2008). The focus of this study was on the lower synchronization branch because it is known from Morse *et al.* (2008) for a plain cylinder undergoing VIV that the free spanwise end condition affects the lower synchronization branch the most, yielding vibration amplitudes much higher than the amplitudes that would be achieved if it were to end with an endplate. To address the shortcomings of the previous studies in this area, numerous wire positions are considered over the full range of angular positions on the cylinder surface from  $\theta = 0^\circ$  to  $180^\circ$  (with respect to the most upstream point of the cylinder), while keeping the characteristics of the oscillation system (such as mass and damping) and the incoming flow properties constant. The oscillation motion and near-wake velocity fields are measured simultaneously to reveal the interplay between the vortex formation and the VIV response of the structure under the surface wire influence. The amplitude, frequency and time traces of structural oscillations are identified along with the associated vortex shedding modes for the entire range of wire locations. These results led to the first-time identification of several VIV response categories depending on the wire location. As an important outcome of this work, the spanwise wire at specific positions is shown to be effective in suppressing or amplifying the VIV of the cylinder in question. In comparison with the oscillation amplitude of the clean cylinder under identical conditions, up to 98 % amplitude reduction and 102 % amplitude increase in cylinder oscillations are shown to be possible in this study through the use of the single spanwise surface wire.

## 2. Experimental set-up

Experiments were conducted in a recirculating water tunnel at the University of Toronto Institute for Aerospace Studies. The main test section of this tunnel is 5000 mm long and has a width of 610 mm and a height of 685 mm. The free-stream turbulence intensity is less than 0.5 % and the flow uniformity is better than 0.3 % within the test section. The test section walls are made out of Plexiglas material to allow visual access to the flow. The current study required the test model, which was mounted to a mechanism above the tunnel, to go through VIV. The top tunnel wall was removed to permit those oscillations, yielding an end condition where the cylinder pierced the water surface.

The test model was a rigid polycarbonate circular cylinder with a diameter of  $D = 50.8$  mm and a length of  $L = 534$  mm, giving a cylinder aspect ratio of  $L/D = 10.5$ . A transparent acrylic wire was tightly stretched and glued on the surface of this cylinder, parallel to its span. The diameter of this wire was  $d = 3.175$  mm, which means the wire-to-cylinder diameter ratio was  $d/D = 0.0625$ . All tests concerning the wire-fitted cylinder (both stationary and free oscillating) were carried out at a free-stream velocity of  $U = 0.186$  m s<sup>-1</sup>, which corresponds to a cylinder-diameter-based Reynolds number of  $Re = 10\,000$ . The surface wire used was larger than the boundary layer thickness forming around an equivalent plain circular cylinder at this Reynolds number. This inference is based on the boundary layer thickness data provided by Aydin *et al.* (2014). For experiments where the VIV response branches of the plain cylinder (without a surface wire) were investigated by collecting the amplitude versus reduced velocity data, a free-stream velocity range of  $U = 0.057$  m s<sup>-1</sup> to  $0.258$  m s<sup>-1</sup> was used, corresponding to a Reynolds number range of  $Re = 3000$  to  $12\,500$ . The angular position of the wire on the cylinder surface was changed by rotating the cylinder–wire arrangement around the longitudinal axis of the cylinder using a computer-controlled, high-precision step motor. The wire angular positions considered in the investigation ranged from  $\theta = 0^\circ$  to  $180^\circ$  ( $\theta = 0^\circ$  being the most upstream point of the cylinder). The angular increment of the wire position was  $0.2^\circ$ ,  $1^\circ$ ,  $2^\circ$  or  $5^\circ$ , depending on the angular resolution needed to detect the

changes in the cylinder response and flow field. Whenever significant changes in cylinder response and/or flow field occurred with a change in wire location, a smaller angular increment was selected. The accuracy of the motorized angular positioning system was  $0.067^\circ$ ; however, the reported angular positions of the wire on the cylinder surface had an uncertainty of  $\pm 1.4^\circ$  due to the added uncertainty in defining the zero-reference angle (i.e. the most upstream point of the cylinder).

The entire length of the model was immersed vertically inside the water channel. Its top end was attached to a mechanism, as shown in [figure 1](#), which permitted the model to vibrate in the cross-stream direction as a result of fluid forcing while preventing motion in the streamwise direction. For tests where the surface-wire-fitted cylinder was kept stationary (non-oscillating), this same mechanism was still utilized, but with the addition of a stopper that prevented structural vibrations. For the stationary cylinder experiments, the lower end of the cylinder was bounded by an endplate, with no gap left between the cylinder and the endplate. The endplate was made out of transparent Plexiglas material of  $0.25D$  thickness. Its streamwise length was  $7.5D$ , and its width covered the entire width of the channel ( $12D$ ). A  $23.6^\circ$  full-depth bevel was put on its upstream end, with the bevel facing the channel floor to minimize disturbances to the inflow. In accord with the recommendations of Stansby (1974), Szepessy & Bearman (1992) and Khoury (2012), the cylinder axis was situated  $3D$  downstream of the leading edge of the endplate. This endplate design is consistent with those used in the previous literature for stationary cylinders (Ekmekci 2006; Ekmekci & Rockwell 2010; Aydin *et al.* 2014; Joshi & Ekmekci 2019). For all experiments involving free oscillations of the cylinder, a gap equal to 13.8 % of the cylinder diameter (a gap spacing of 7 mm) was left between the bottom end of the cylinder and the endplate to induce conditions of a free-ended cylinder in accord with Morse *et al.* (2008). In § 3.2, the VIV response of the plain cylinder with this end condition will be compared with the results from this reference to show that this gap left beneath the bottom end of the cylinder was sufficient to generate the response of a free-ended cylinder. The two-dimensionality of the flow field with this test set-up was assessed for the oscillating cylinder and proven to be sufficient in Vaziri (2021). The Froude number based on the cylinder length was  $Fr_L = U/\sqrt{gL} = 0.08$ , indicating a subcritical flow in the water channel. Also, the maximum elevation changes of the water around the cylinder were observed to be very small (close to the approximations provided by Hay 1947 and Chaplin & Teigen 2003). Therefore, the effects associated with free-surface distortions on the response of the cylinder can be neglected in accord with Gonçalves *et al.* (2013). The channel blockage ratio for the experimental set-up was 5.8 %.

To conduct free-oscillation experiments, a unique mechanism was designed with attention to minimizing the mass ratio  $m^*$  and damping ratio  $\zeta$  of the system. This mechanism was sitting atop the water channel, as seen in the sketch in [figure 1](#). This mechanism consisted of a rotary step motor to which the cylinder was attached, a mounting square where the step motor and two supporting shafts were connected, two linear extension springs, two spring holders and four air bushings. The springs were placed between the mounting square and the spring holder on each side of the model. The use of air bushing technology in this set-up reduced the structural friction significantly while constraining the cylinder–wire model to move only in the transverse direction (perpendicular to the flow direction). The rotary step motor, mounting square and two supporting shafts were the components that moved with the cylinder while the spring holders and air bushings were fixed to the tunnel. During calibration of the mechanism in air, the response matched with the response of a damped harmonic oscillator with an average correlation coefficient of 0.953, signifying that the mechanism used behaves as

## *Effects of a single spanwise surface wire*

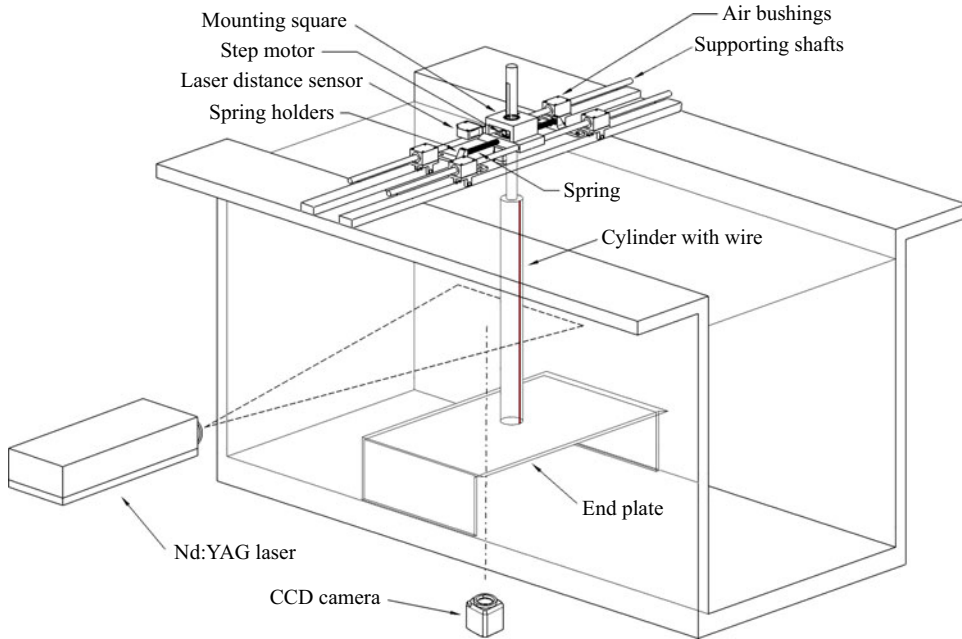


Figure 1. Three-dimensional sketch of the experimental set-up.

a linear system. A detailed discussion of this mechanism and the determination of the damping ratio  $\zeta$  and natural frequency  $f_n$  of the system via a ‘pluck test’ can be found in Vaziri (2021). The free-oscillation system used in the present study, as a whole, had a mass ratio of  $m^* = 2.581$ , a damping ratio of  $\zeta = 0.027$  and its natural frequency was  $f_n = 0.36$  Hz.

A high-resolution laser distance sensor (Wenglor CP24MHT80) was mounted at a fixed position on top of the channel (see figure 1) to capture the instantaneous position of the cylinder with no contact. Its output voltage was sampled at a frequency of 1000 Hz. The uncertainty of the cylinder position, captured by this sensor, is  $0.025D$ , and the uncertainty associated with the frequency of the acquired oscillation motion of the cylinder is  $\pm 0.005$  Hz.

The motion of the cylinder undergoing free vibrations can be highly irregular for some surface wire positions. As a result, the amplitude of oscillations cannot be simply defined as half of the difference between the maximum (peak) and minimum (valley) points in the displacement signal. To account for the variations in peaks and valleys, the present study reported the cylinder amplitude as half of the distance swept by the cylinder between the overall upper and lower limits of the oscillation motion. The overall upper limit was defined as the average value of peaks  $\bar{y}_p$  plus the standard deviation of the peak values  $\sigma_p$ . Similarly, the overall lower limit was defined as the average value of valleys  $\bar{y}_v$  minus the standard deviation of valley values  $\sigma_v$ . To employ this method, a peak detection algorithm was applied to the time series of the displacement signal to determine the peaks  $y_p$  and valleys  $y_v$ . Then, the following expression was used to determine the oscillation amplitude normalized by the cylinder diameter:

$$A^* = \frac{(\bar{y}_p + \sigma_p) - (\bar{y}_v - \sigma_v)}{2D}. \quad (2.1)$$

High-image-density PIV was used to capture the velocity field information in the near wake. For this technique, the flow was seeded with neutrally buoyant hollow-glass particles, having a nominal mean diameter of 8 to 1  $\mu\text{m}$ . Illumination of the flow field was achieved using a double-pulsed Nd:YAG laser system with a maximum energy output of 20 mJ pulse<sup>-1</sup> at a wavelength of 532 nm. A series of cylindrical and spherical lenses converted the laser-beam output of this system to a laser sheet, which illuminated the planar flow region of interest. In all tests, a sequence of 1000 image pairs was recorded at a rate of 14.5 frame pairs per second via a PowerView Plus 2 MP CCD camera, which had an array size of 1600  $\times$  1200 pixels. This sampling rate corresponded to approximately 69 s of sequential data acquisition. For tests involving cylinder vibrations, the PIV data acquisition was synchronized with the laser distance sensor data employing a LaserPulse Model 610035 synchronizer. As seen in [figure 1](#), the laser sheet was aligned horizontally, and the CCD camera was placed vertically beneath the water channel. The acquired field of view during the free-oscillation tests covered  $2.1D$  in the streamwise direction starting from the cylinder's most downstream point and had a total length of  $3.2D$  in the cross-stream direction. This field of view included the downstream regions of both shear layers separating from the oscillating cylinder. For the stationary cylinder, the field of visualization was  $3D \times 2.2D$ , which also contained the two shear layers separating from the cylinder. During image processing, an interrogation window size of  $32 \times 32$  was used with an overlap of 50 %, producing a total of 7227 velocity vectors ( $99 \times 73$ ) for both the free-oscillation and stationary cylinder tests. Based on the dimensions of the field of view, the velocity vector resolution for the PIV data was approximately  $0.0321D$  for the free-oscillation tests and  $0.0297D$  for the stationary cylinder tests. The dominant frequency of the streamwise and transverse velocity components ( $f_u$  and  $f_v$ ) over the global flow field was determined by applying fast Fourier transformation (FFT) to PIV snapshots. The selected size of the visualization field provided sufficient spatial resolution for both velocity vectors and the autospectral density amplitude of velocity fluctuations. The uncertainty associated with the frequency of velocity fluctuations obtained from the FFT of the PIV data was  $\pm 0.007$  Hz.

### 3. Results

The focus of the present study is on developing an understanding of the structural oscillations and vortex shedding characteristics of a surface-wire-fitted, elastically mounted cylinder moving in the transverse direction with low mass-damping and one free end. The wire influence is assessed for having a single wire at different locations on the surface of the cylinder. First, before studying the impact of the wire on the elastically mounted cylinder that undergoes free transverse oscillations, the influence of the wire on the near-wake flow structure of the stationary cylinder for varying wire positions will be discussed in § 3.1 to form the baseline scenario. Then, in § 3.2, the oscillation response of the plain (untripped) cylinder as a function of reduced velocity for the end conditions and system parameters used in the VIV tests of this study will be characterized and compared with a similar previous investigation. Section 3.3 is where the results related to the wire-fitted cylinder undergoing free-oscillation motion will be presented. Therein, the § 3.3.1 will focus on the oscillation characteristics of the wire-fitted cylinder (again for various wire locations), while in § 3.3.2 the unsteady near-wake flow structure will be discussed for the same oscillating cylinder with the surface wire at different locations, and the vortex shedding frequency in comparison with the frequency of cylinder oscillations

will be examined to explore the link between the structural oscillations and the flow field characteristics. Finally, in § 4, the conclusions will be outlined.

### 3.1. *The surface-wire-fitted cylinder under stationary condition*

For a stationary circular cylinder, it is known that several critical angular locations can be defined on its surface for the application of a large-scale wire. Most of these critical locations are related to distinct changes in the trend of the non-dimensional vortex shedding frequency (i.e. Strouhal number) with the change of the wire location, as shown by Nebres & Batill (1993). Two specific critical angles are related to the attenuation and intensification of the Kármán instability. They can be distinguished as locations where the application of the wire significantly attenuates or intensifies the spectral amplitude of velocity fluctuations at the Kármán frequency, as addressed by Ekmekci (2006), Ekmekci & Rockwell (2010) and Aydin *et al.* (2014). Critical locations generally depend on the wire diameter to cylinder diameter ratio ( $d/D$ ) and the Reynolds number (Nebres & Batill 1993; Aydin & Ekmekci 2014). Among all the critical locations, those that are based on the spectral amplitude of velocity fluctuations associated with the Kármán instability are called the first and second critical locations  $\theta_{c1}$  and  $\theta_{c2}$ . A brief overview of these two critical angles and their essential features were discussed in the introduction section earlier.

For the  $d/D$  ratio and Reynolds number used in the present study, the first critical angle  $\theta_{c1}$  ranged from  $41.2^\circ$  to  $43^\circ$ , and the second critical angle  $\theta_{c2}$  ranged from  $50^\circ$  to  $80^\circ$ . These angular ranges are determined in the current study by evaluating the autospectra of the flow velocity taken from the PIV measurements in the near wake. It should be noted that the angular resolution of the test cases in these PIV experiments was refined to  $0.2^\circ$  around these critical locations. The  $\theta_{c1}$  and  $\theta_{c2}$  locations obtained in the present study show good correspondence with the values reported earlier by Joshi & Ekmekci (2019), where the range of  $\theta_{c1}$  was reported as  $42^\circ$  to  $44.5^\circ$ , and the range of  $\theta_{c2}$  was  $52^\circ$  to  $80^\circ$  for the same  $d/D$  ratio and Reynolds number. The slight discrepancy in the reported ranges of critical angles between the present study and Joshi and Ekmekci's study can be attributed to the error in defining the  $\theta = 0^\circ$  wire location ( $\pm 1.4^\circ$  in the present study) and the arrangement of the experimental set-up (i.e. use of the open channel flow in the present study versus closed water tunnel in the Joshi and Ekmekci's work).

The contour patterns in figure 2 illustrate the autospectral density of streamwise velocity fluctuations at the predominant Kármán frequency,  $S_u(St)$ , for the case where the wire is at the second critical position  $\theta_{c2} = 58.2^\circ$  and the case representing the non-tripped scenario ( $\theta = 180^\circ$ ). It is known from previous work on stationary cylinders that, being at the base region, a surface wire at  $\theta = 180^\circ$  shows no significant influence on the strength and coherence of the Kármán instability (Nebres & Batill 1993; Ekmekci & Rockwell 2010). Also, in this figure, the global contour patterns of autospectral density are shown for the first critical angle  $\theta_{c1} = 41.6^\circ$  at the frequency corresponding to the bistable flow separation, as identified by Ekmekci & Rockwell (2010). To obtain these results, first, the autospectral density of the streamwise velocity fluctuations was determined at a total of 7227 locations over the global near-wake region from the PIV data. Then, the autospectral magnitude corresponding to the frequency in question was extracted from each spectrum and shown as a contour plot. The frequencies corresponding to the autospectral density contours in figure 2 are indicated in the insets in terms of Strouhal number  $St$ . It should be noted here that the value of the dominant  $St$  varies as a function of the wire application location  $\theta$ , as reported in previous investigations (Ekmekci & Rockwell 2010; Aydin *et al.* 2014). When the wire is applied at the first critical angle  $\theta_{c1}$ , figure 2 shows that the bistable separation of the shear layer induces moderate levels of low-frequency activity

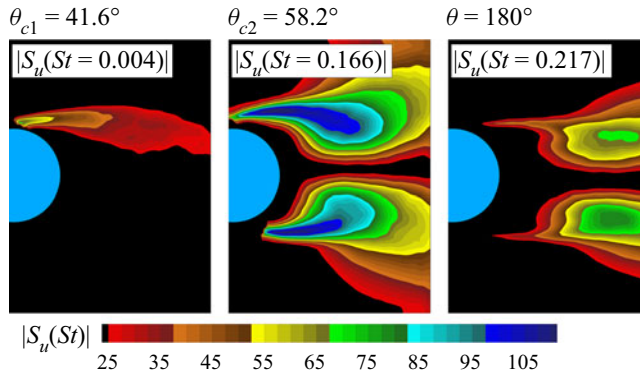


Figure 2. Contours of autospectral density of the streamwise velocity fluctuations at the specific Strouhal number value indicated in the inset for the stationary cylinder fitted with the surface wire at the first  $\theta_{c1}$  and second  $\theta_{c2}$  critical angles, and at  $\theta = 180^\circ$  (representing the clean cylinder). Minimum and incremental values of the contours are  $[|S_u(St)|]_{min} = 25 \text{ mm s}^{-1}$  and  $\Delta[|S_u(St)|] = 2.5 \text{ mm s}^{-1}$ .

(at  $St = 0.004$ ) in the upper shear layer separating from the wire side of the cylinder; however, a dominant frequency corresponding to the Kármán vortex shedding did not exist for this case in the entire near wake, implying an attenuation in the Kármán vortex shedding process. The wire at the second critical angle  $\theta_{c2}$  enhances the strength and coherence of the Kármán instability as apparent from the existence of high autospectral amplitudes in the near wake. These results are in total agreement with the results shown earlier for a wire-fitted stationary cylinder by Ekmekci & Rockwell (2010).

From the global spectrum results discussed in this section, it is apparent that the surface wire used in this study affects the Kármán vortex shedding substantially for the stationary cylinder. Plausibly, it is not unreasonable to expect the spanwise wire to affect the oscillation response of a cylinder undergoing VIV significantly. For example, the observed time-averaged attenuation of the Kármán vortex shedding with the wire at  $\theta_{c1}$  position for the stationary cylinder suggests that VIV may be suppressed when the wire is placed at this critical location. With similar reasoning, because of the observed enhancement in the coherence and strength of the Kármán vortex shedding with the placement of the wire at  $\theta_{c2}$  in the stationary cylinder case, the wire at the same critical location may be expected to aggravate the VIV response of an elastically mounted cylinder. However, as will be seen in § 3.3, the effects of the spanwise wire on the free-oscillation motion of the cylinder are not as expected at the critical angles of the stationary cylinder. Other critical locations will be identified where the placement of the wire substantially affects the characteristics of the cylinder oscillations and the flow field.

### 3.2. The VIV response of the plain cylinder

Figure 3 shows the variation of the vibration amplitude  $A^*$  with reduced velocity  $U^*$  for the plain version of the cylinder used in this study (i.e. cylinder without a wire) as it undergoes VIV with the end conditions and system parameters used throughout this investigation compared with those obtained by Morse *et al.* (2008). In the referenced work, the top end of their submerged plain cylinder was bounded by the free surface of the water channel as in the present study, while different end conditions were considered for the lower end. The response plots for two of these end conditions are included in figure 3. These are: the case with an unattached endplate, leaving a gap of 2 mm (which corresponds to

## Effects of a single spanwise surface wire

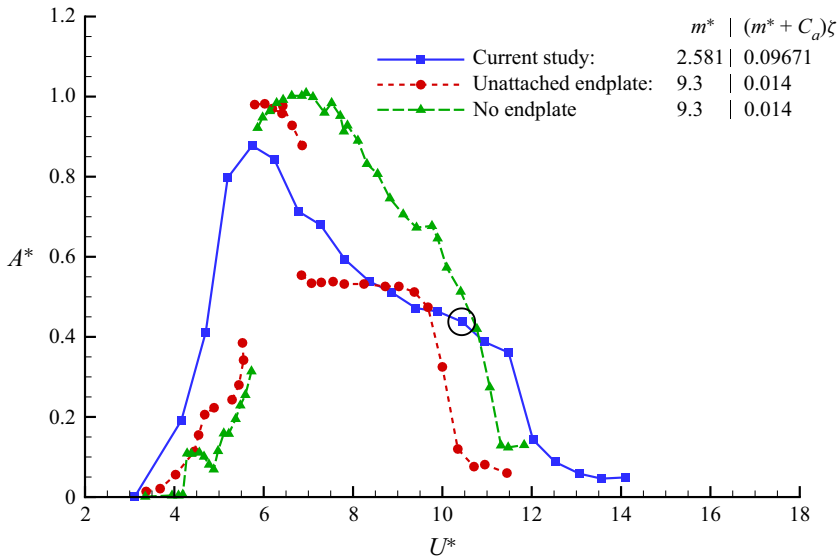


Figure 3. Comparison of the vibration response amplitude ( $A^*$ ) of the plain cylinder as a function of reduced velocity ( $U^*$ ). Blue square: current study ( $m^* = 2.581$ ,  $(m^* + C_d)\zeta = 0.097$ , an unattached endplate with a gap equal to 13.8% of the cylinder diameter); red circle: Morse *et al.* (2008) ( $m^* = 9.3$ ,  $(m^* + C_d)\zeta = 0.014$ , an unattached endplate with a gap equal to 4% of the cylinder diameter); green triangle: Morse *et al.* (2008) ( $m^* = 9.3$ ,  $(m^* + C_d)\zeta = 0.014$ , no endplate).

a distance of 4% of the cylinder diameter) at the bottom end of the cylinder, and the case with no endplate. They noticed that the free vibration response of the cylinder when the endplate is unattached with such a small gap is nearly equivalent to the response for having the plate attached to the cylinder, with the typical initial, upper and lower response branches (as seen in the response plot corresponding to the unattached plate case taken from Morse *et al.* 2008 in figure 3). However, with no endplate, the free-ended cylinder depicts remarkable distinctions in its response plot. While the peak amplitude in the upper branch stays almost unchanged, the vibration amplitude of the case with no endplate shows a gradual decrease from this peak as  $U^*$  is increased, with this trend continuing in the lower branch. Also, no sign of a jump is distinguishable between the upper and lower branches for the no-endplate response. An important finding in their study is that the vibration response of the cylinder with the unattached endplate becomes equivalent to the response of the free-ended cylinder (with no endplate at all), provided that the unattached plate case has a large enough gap. This gap was estimated in their study to be around 15% of the cylinder diameter, which means that for a 50.8 mm-diameter cylinder, the gap should be close to approximately 7.6 mm or above to produce the vibration response of a free-ended cylinder. In the present investigation, leaving a gap of 7 mm between the free end of the cylinder and the endplate yielded the response plot given in figure 3, which exhibits good correspondence with the no-endplate case of Morse *et al.* (2008). It shows a gradual decrease from the peak amplitude in the upper branch until the end of the lower branch, with no distinct transitional jump between the two branches. Because the response data in the present study are from a system with slightly higher mass-damping than the no-endplate case of Morse *et al.* (2008), the amplitudes in the upper branch are smaller in the present study compared with theirs. Also, having a smaller mass ratio compared with their results in the range of synchronization being

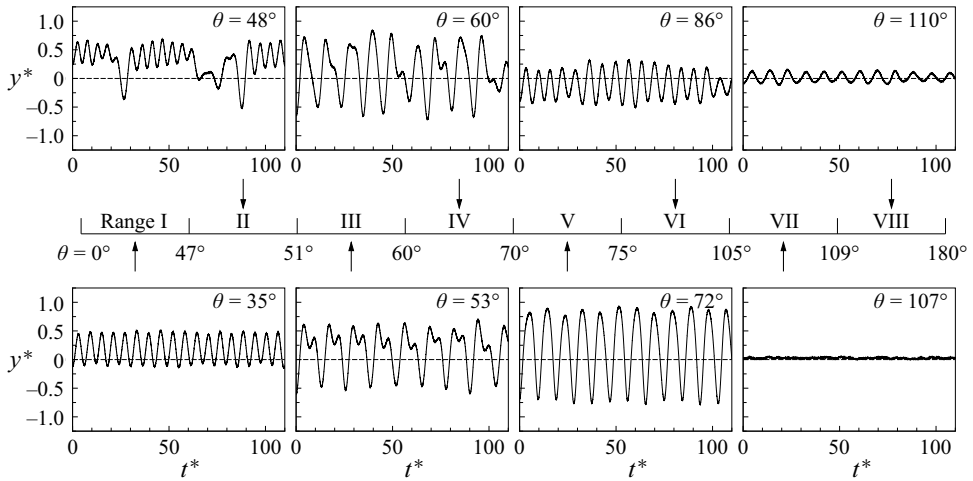


Figure 4. Time traces of the cylinder position for the application of the wire at different angular locations on the cylinder surface. The axis of angular values, where the range divisions are shown, is not to scale.

wider in the present, in accord with Govardhan & Williamson (2000). Consequently, a one-to-one comparison of the response plots between the present study and the no-endplate case of Morse *et al.* (2008) shows that the 7 mm gap left between the lower end of the cylinder and the unattached endplate is sufficient to produce the response of a free-ended cylinder.

From the discussions above, it can be seen that the effect of the free-end condition on the VIV of a cylinder is that it significantly increases the oscillation amplitudes, particularly in the lower branch, compared with the end condition of an attached endplate (or an unattached endplate with a small gap). In the present study, a reduced velocity of  $U^* = 10.44$  is considered, which lies within the lower branch of synchronization, for investigating the wire effects on the vortex shedding and oscillation of the free-ended cylinder. This point in the lower branch is marked by a circle symbol in figure 3. Note that, at this  $U^*$  value, the sensitivity of the plain cylinder's oscillation amplitude to small variations in  $U^*$  is low (such that a variation of approximately 5% in the value of  $U^*$  leads to a small change of 5.6% in the oscillation amplitude).

### 3.3. The surface-wire-fitted cylinder undergoing free-oscillation motion

#### 3.3.1. Cylinder oscillation patterns

Time traces of the cylinder position are shown in figure 4 with the spanwise surface wire in question at different angular locations. In all plots, the horizontal axis depicts a total of 30 s in non-dimensional form  $t^* = tU/D$  for visual clarity of the oscillation patterns, although the acquired displacement signal of the cylinder was longer (180 s). The vertical axis in the plots shows the position of the cylinder in non-dimensional form  $y^* = y/D$ . Here,  $y^* = 0$  in the vertical axis corresponds to the equilibrium position of the model in still water, and the positive  $y^*$  direction shows cylinder displacements in the direction of the wire-fitted side of the cylinder. Based on the characteristics of the oscillation motion, the wire angular position is divided into eight angular ranges in figure 4.

For the wire angular positions that fall in range I ( $0^\circ \leq \theta < 47^\circ$ ), the position around which the cylinder oscillates shifts toward the wire-fitted side of the cylinder while the

cylinder displacements follow a regular sinusoidal pattern. In [figure 4](#),  $\theta = 35^\circ$  is provided as a representative case from this first range. In range II ( $47^\circ \leq \theta < 51^\circ$ ), the regular sinusoidal response of the cylinder motion is disrupted intermittently by large-amplitude displacements. In [figure 4](#), the oscillation pattern for  $\theta = 48^\circ$  is given as a sample case from this range. Because the cylinder response in this second range of wire positions is a combination of low-amplitude sinusoidal and high-amplitude disturbed motions that appear randomly, this angular range II can be considered a critical range for wire placement. As  $\theta$  increases within this range starting from the wire position of  $\theta = 47^\circ$ , the disturbed motion appears more and more frequently, and eventually gives way to another pattern starting at  $\theta = 51^\circ$ . For range III ( $51^\circ \leq \theta < 60^\circ$ ), a non-sinusoidal but distinct oscillation pattern, repeating at every period, is observed, as depicted for the sample case of  $\theta = 53^\circ$  in [figure 4](#). Starting from  $\theta = 60^\circ$ , the cylinder with the wire in the angular range IV ( $60^\circ \leq \theta < 70^\circ$ ) depicts a motion consisting of quasi-sinusoidal displacements along with the sporadic appearance of irregular oscillation patterns. When the surface wire is placed within range V ( $70^\circ \leq \theta < 75^\circ$ ), the cylinder shows a response that is nearly sinusoidal. This pattern is not symmetric around the equilibrium position such that the oscillation pattern has a wider peak for movements on the wire side (for positive values of  $y^*$ ). In range VI ( $75^\circ \leq \theta < 105^\circ$ ), the oscillation pattern has a quasi-uniform character, with the appearance of small-amplitude modulations between cycles. When the wire is placed at any of the angular positions in range VII ( $105^\circ \leq \theta < 109^\circ$ ), the amplitude of the cylinder oscillations diminishes substantially. In this seventh range, the largest attenuation in the amplitude of the cylinder motion occurs when the wire is at around  $\theta = 107^\circ$ , where, as shown in [figure 4](#), the cylinder stays at its equilibrium state with almost no oscillatory motion. For wire positions of range VIII ( $109^\circ \leq \theta \leq 180^\circ$ ), the oscillatory motion for the cylinder restarts with a nearly sinusoidal pattern, as seen in [figure 4](#) for the representative scenario of  $\theta = 110^\circ$  from this range, and as the wire approaches  $\theta = 180^\circ$ , the oscillation pattern resembles more and more the regular sinusoidal pattern of the clean cylinder (with no wire).

### 3.3.2. *Cylinder oscillation frequency*

The dominant frequency of cylinder oscillations  $f_d$  is observed to change significantly depending on the wire angular position  $\theta$ . This variation is depicted in [figure 5](#), where the dominant frequency of the cylinder motion  $f_d$  is given in non-dimensional form by normalizing it with the natural frequency of the oscillating system  $f_n$  in still water (i.e.  $f_d^* = f_d/f_n$ ). The non-dimensional dominant frequency of oscillations for the clean (untripped) cylinder, which corresponds to a value of  $f_d^* = 1.29$ , is also marked in [figure 5](#) with a horizontal dashed line as the baseline to compare with. As discussed earlier, the cylinder depicts a regular sinusoidal motion when the wire is placed in the angular range I ( $0^\circ \leq \theta < 47^\circ$ ). In this range, as the angular position of the wire is increased starting from  $\theta = 0^\circ$  until approximately  $\theta = 15^\circ$ , the frequency of the cylinder oscillations remains constant at a value of  $f_d^* = 1.28$ , which is only slightly below  $f_d^*$  of the clean cylinder. After  $\theta = 15^\circ$ , the frequency of oscillations in range I gradually increases as the wire angular position increases. When the wire is placed in the angular range II ( $47^\circ \leq \theta < 51^\circ$ ), a single dominant frequency is not discernible for the cylinder oscillations because, as seen in [figure 4](#), the sinusoidal cylinder motion is disrupted by the random appearance of irregular oscillations spanning a wide range of amplitudes and frequencies. For this reason, the second  $\theta$  range in the  $f_d^* - \theta$  plot, given in [figure 5](#), is filled with a hatch pattern. For angular locations of range III ( $51^\circ \leq \theta < 60^\circ$ ), the displacement motion has two dominant frequencies, as marked in [figure 5](#). Both dominant frequencies in range III increase with

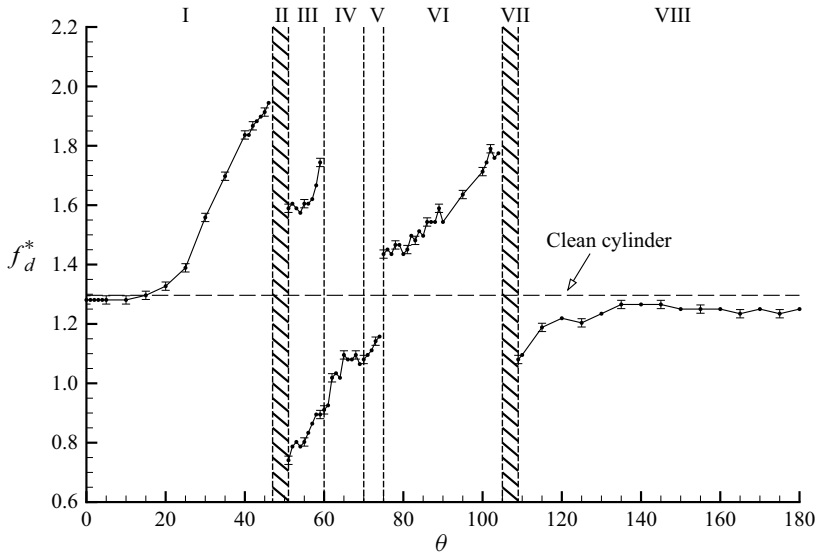


Figure 5. Variation of the frequency of cylinder oscillations in non-dimensional form ( $f_d^* = f_d/f_n$ ) with the wire angular position. The horizontal dashed line indicates the non-dimensional frequency of the oscillation motion for the clean (untripped) cylinder.

an increase in the angular location of the wire placement. The displacement response has one dominant frequency at angular locations in the ranges IV, V and VI, where the frequency of oscillations increases with the wire angle. Here,  $f_d^*$  shows a sudden increase at  $\theta = 75^\circ$ , which is the start of range VI ( $75^\circ \leq \theta < 105^\circ$ ). In the angular range VII ( $105^\circ \leq \theta < 109^\circ$ ), there is no dominant frequency because the cylinder does not undergo any discernible oscillation motion (as seen in figure 4). Thus, this range is also covered with a hatch pattern in figure 5. It should be noted here that the hatched areas for the angular ranges II and VII in figure 5 have different interpretations. In the angular range II ( $47^\circ \leq \theta < 51^\circ$ ), the cylinder motion consists of a combination of sinusoidal and irregular motions (as seen in figure 4) encompassing a wide range of amplitudes and frequencies, so a specific frequency cannot be selected as the prevailing one. However, in range VII ( $105^\circ \leq \theta < 109^\circ$ ), the cylinder does not have a discernible oscillation motion, so that a dominant frequency is not detectable. For the angular positions of the wire in range VIII ( $109^\circ \leq \theta \leq 180^\circ$ ), a dominant frequency for cylinder oscillations is perceptible again, and figure 5 shows that this frequency is close to the oscillation frequency of the clean cylinder, particularly for  $\theta \geq 135^\circ$ .

To explore the possible temporal variations in the dominant frequency of cylinder oscillations when the surface wire is applied, the short-time Fourier transform (STFT) has been applied to the cylinder displacement data for different wire placement positions. Figure 6 shows the time–frequency spectrogram of the cylinder oscillations, determined via STFT, for the same wire angular locations provided earlier in figure 4. Each angle in figure 6 is representative of the situation seen within one of the eight angular ranges. In these spectrogram plots, the horizontal axis shows the non-dimensional time  $t^* = tU/D$ , and the vertical axis shows the non-dimensional displacement frequency  $f_d^*$  of the wire-fitted cylinder. The colour-coded contour levels indicate the magnitude of the autospectral density at a given frequency and time (i.e.  $S_{y^*}(t^*, f_d^*)$ ). The colour maps for

## Effects of a single spanwise surface wire

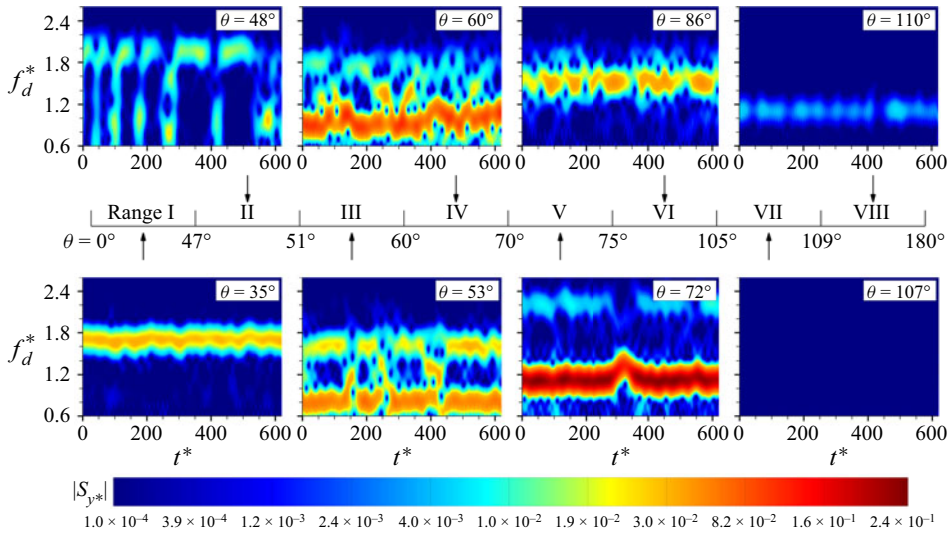


Figure 6. Time–frequency spectrogram of the cylinder oscillations for having the wire at different angular locations on the cylinder surface. The axis of angular values, where the range divisions are shown, is not to scale.

the amplitude of autospectral density in the spectrogram plots of figure 6 are provided in logarithmic scale to demonstrate the differences in spectral amplitudes for different  $\theta$  ranges. Therein, the red regions mark the highest spectral amplitudes, while the blue regions mark the lowest amplitudes. In order to depict a holistic picture of the frequency variation with time, the frequency spectrogram plots presented in figure 6 are shown over a longer period compared with the displacement time traces given earlier in figure 4.

In range I ( $0^\circ \leq \theta < 47^\circ$ ), there is only one dominant value for the frequency  $f_d^*$ , and this frequency is unchanged with time, as apparent from the time–frequency spectrogram of the representative case ( $\theta = 35^\circ$ ) given in figure 6. For range I, the presence of one constant frequency for the largest spectral magnitudes over the entire time domain is consistent with the regular oscillation motion seen in figure 4. For range II ( $47^\circ \leq \theta < 51^\circ$ ), as seen for the representative case of  $\theta = 48^\circ$  in figure 6, the dominant frequency of the cylinder oscillations scatters over a wide range depending on the time. This time-varying nature of the frequency  $f_d^*$  is consistent with the intermittent switching of the oscillation mode observed in figure 4 for this range. The short periods during which the dominant frequency of the cylinder oscillations  $f_d^*$  has a fixed value correspond to the times when the cylinder undergoes regular sinusoidal oscillations, and the times when the dominant frequency  $f_d^*$  is spread over a wide range of values in the spectrogram plot correspond to the times when the cylinder motion becomes irregular, spanning a wide range of amplitudes and frequencies. It should be emphasized here that these characteristics in the time–frequency domain of the sample case ( $\theta = 48^\circ$ ) are observed for all angular locations within range II ( $47^\circ \leq \theta < 51^\circ$ ).

When the wire is located in range III ( $51^\circ \leq \theta < 60^\circ$ ), as can be observed from the spectrogram plot of the  $\theta = 53^\circ$  case in figure 6, two dominant frequencies co-exist at any given time in the displacement signal of the cylinder. This result implies that the cylinder oscillations consist of the superposition of two sinusoidal motions, which is consistent with the displacement pattern presented earlier in figure 4 for this third angular range. For  $\theta = 53^\circ$  in figure 6, it should be noted that, in the time–frequency spectrogram of the

cylinder oscillations, there exists a few occasions where the dominant frequency  $f_d^*$  varies over a range of values. During these short time periods, a disturbed motion exists, which occurs randomly within the angular locations of range III.

In range IV ( $60^\circ \leq \theta < 70^\circ$ ), as the spectrogram plot of the  $\theta = 60^\circ$  case in [figure 6](#) shows, the predominant frequency of cylinder oscillations shows a slight variation with time within a narrow range of frequencies. However, there is only one dominant frequency at each time step for the displacement motion. These observations comply with the oscillation pattern seen earlier in [figure 4](#) for range IV, which consists of quasi-sinusoidal oscillations with the sporadic appearance of non-sinusoidal patterns. The variation in the dominant oscillation frequency becomes smaller with increasing wire angular location in this range. Consequently, examining the cylinder motion for different angular locations in this range shows that the irregular motion manifests less frequently as the wire angular location increases.

For the next range of angular locations, range V ( $70^\circ \leq \theta < 75^\circ$ ), the time–frequency spectrogram analysis shows continuous contours of very high autospectral magnitudes at one fixed frequency, as seen for  $\theta = 72^\circ$  in [figure 6](#). This signifies a regular, coherent oscillation motion for the angular locations of range V. One noticeable feature in the spectrogram plot of  $\theta = 72^\circ$  in [figure 6](#) is the appearance of a short-time small increase in the dominant frequency at around  $t^* = 320$ , which is accompanied by a temporary drop in the amplitude of the cylinder oscillation. Such frequency variations in range V, however, occur very rarely.

In range VI ( $75^\circ \leq \theta < 105^\circ$ ), the dominant frequency of the cylinder oscillations remains constant, while the spectral magnitude of cylinder displacements at the dominant frequency shows changes with time, as can be seen in the spectrogram plot of  $\theta = 86^\circ$  in [figure 6](#). Such fluctuations in the spectral amplitude of the dominant frequency suggest the presence of variations in the coherency of the oscillation motion. The quasi-uniform character of the oscillation pattern with small-amplitude modulations, seen before for range VI in [figure 4](#), complies with this observation.

When the wire is placed at angular locations of range VII ( $105^\circ \leq \theta < 109^\circ$ ), there is no regular oscillation motion, as seen earlier for  $\theta = 107^\circ$  in [figure 4](#). As a result, there is no dominant frequency, and the spectral magnitude of the displacements is at the noise level for this range, as observed in the spectrogram plot of  $\theta = 107^\circ$  in [figure 6](#).

The time–frequency spectrogram of cylinder oscillations at  $\theta = 110^\circ$  in [figure 6](#) reveals the existence of a dominant frequency since the oscillation motion resumes in the angles of range VIII ( $109^\circ \leq \theta < 180^\circ$ ), as depicted in [figure 4](#). Although the spectral magnitude has low values and continuously fluctuates with time at  $\theta = 110^\circ$ , as the wire is placed at the higher angular locations of range VIII, the spectral magnitude becomes constant with time (not shown in [figure 6](#)), and the time traces of the cylinder displacement turn into perfect sinusoids.

To further examine the frequency characteristics of cylinder oscillations, the autospectral density of cylinder displacements  $S_{y^*}(f_d^*)$  was evaluated using the classical FFT analysis. These results are presented in [figure 7](#) for every  $1^\circ$  increment of  $\theta$  within the ranges I to IV, where the scale of the vertical axis is the same in each plot to ease the comparison of the spectral amplitudes. [Figure 7\(a\)](#) presents the displacement spectra for four angles at the end of range I as a basis for comparison. As mentioned earlier, the cylinder undergoes a uniform sinusoidal oscillation for every wire angular location in range I. It is, therefore, observed that there is only one peak in the spectra of the displacement signal in [figure 7\(a\)](#), and this observation confirms the existence of only one dominant frequency in the first angular range. For all wire angular locations of range II ( $47^\circ \leq \theta < 51^\circ$ ), small spectral amplitudes are distributed over many frequencies, and

## Effects of a single spanwise surface wire

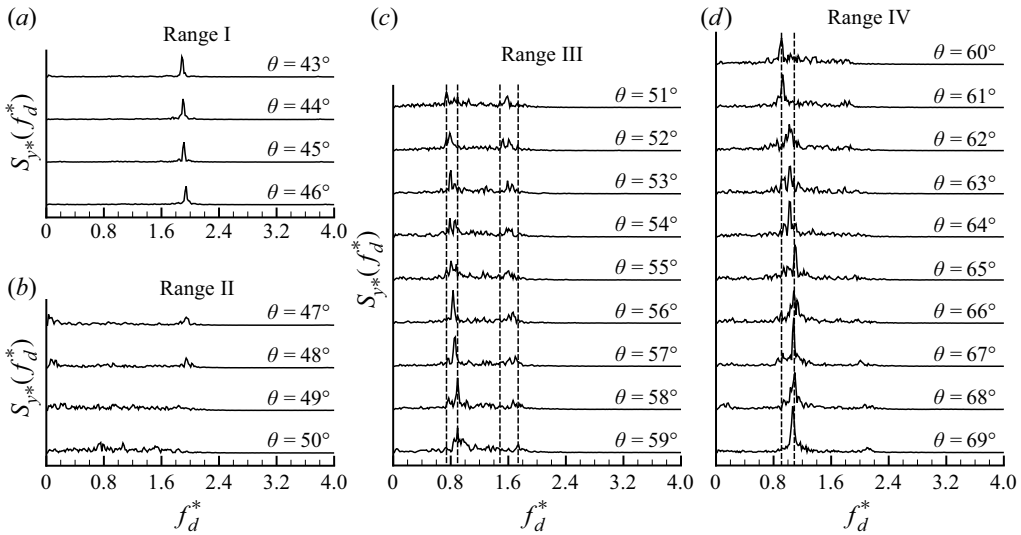


Figure 7. Autospectral density of the cylinder displacements,  $S_{y^*}(f_d^*)$ , for select locations of the wire in: (a) range I ( $0^\circ \leq \theta < 47^\circ$ ), (b) range II ( $47^\circ \leq \theta < 51^\circ$ ), (c) range III ( $51^\circ \leq \theta < 60^\circ$ ) and (d) range IV ( $60^\circ \leq \theta < 70^\circ$ ).

therefore, no dominant frequency can be selected, as apparent from the spectra provided in figure 7(b). This result complies with the time traces of the cylinder position given in figure 4 and the time–frequency spectrogram of the cylinder oscillations shown in figure 6 for range II, where intermittent switching between seemingly sinusoidal and disturbed cylinder motions was revealed. Although the cylinder fitted with the wire at the angular locations of range II undergoes short periods of somewhat sinusoidal-looking oscillations, a single frequency is still not discernible for this range, as observed in figure 7(b).

In the wire angular range III ( $51^\circ \leq \theta < 60^\circ$ ), the co-existence of dual frequencies in the time–frequency spectrogram of the cylinder oscillations, seen in figure 6, agrees with the FFT spectra of the cylinder displacements, given in figure 7(c). For all  $\theta$  in figure 7(c), two dominant frequencies are discernible in the spectra of the cylinder displacements. This indicates that the oscillation motion of the cylinder in this  $\theta$  range mainly consists of a superposition of two sinusoidal motions with different frequencies, which was also apparent from the time traces of the cylinder position given in figure 4 for the representative case of  $\theta = 53^\circ$ . This twin-peak phenomenon in cylinder motion derives from the vortex shedding mechanism prevalent in this  $\theta$  range, as will be discussed in § 3.4. One interesting observation that comes out of figure 7(c) is that the two dominant frequencies increase with increasing wire angular position. The vertical dashed lines in figure 7(c) mark the minimum and maximum values of these frequencies. Furthermore, as the angular position of the wire increases, the spectra demonstrate a gradual transfer of energy from the larger-frequency motion to the lower-frequency motion, eventually yielding a single-peak spectrum at  $\theta = 60^\circ$ , which is the start of the fourth range.

In the wire angular range IV ( $60^\circ \leq \theta < 70^\circ$ ), the cylinder displacement data for  $\theta = 60^\circ$ , given earlier in figure 4, displayed a pattern consisting of both sinusoidal and irregular patterns, which was further supported by the time–frequency spectrogram presented in figure 6 for the same  $\theta$ . To further elaborate on this interesting observation, the autospectral density of the cylinder displacement is presented in figure 7(d) for varying  $\theta$  in range IV. In this range, a slight gradual increase in the dominant frequency of cylinder oscillations is discernible with an increase in the angular position of the surface wire from

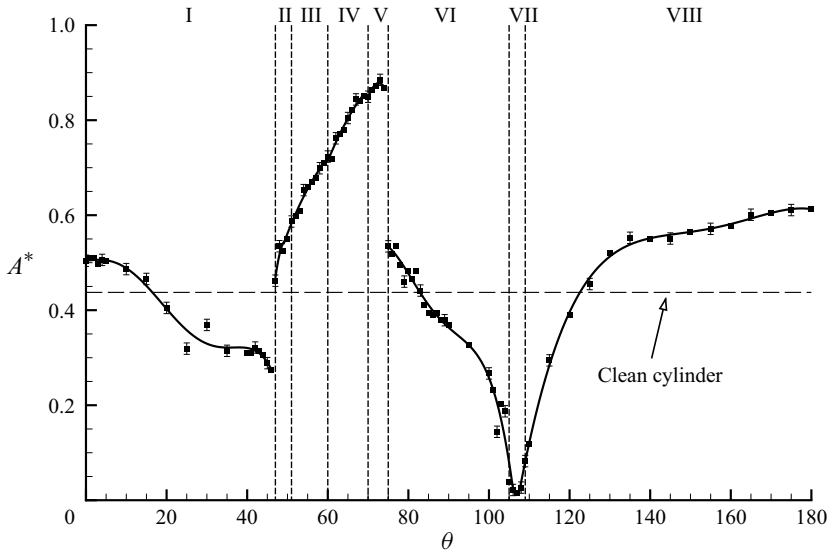


Figure 8. Variation of the non-dimensional amplitude of oscillations  $A^*$  with the wire angular position  $\theta$ . The horizontal dashed line indicates the oscillation amplitude of the clean cylinder, which has the value of  $A^* = 0.44$ . The uncertainty is the same for all cases and is marked on the plot for some data points as a reference.

$\theta = 60^\circ$  to  $\theta = 65^\circ$ , after which the dominant frequency remains constant. This aspect was also visible in figure 5 for range IV. Furthermore, as the wire angle increases, the small, non-dominant spectral amplitudes gradually decrease while the spectral amplitude of the dominant frequency increases, suggesting lessening in the irregular motion as the wire angular location increases.

### 3.3.3. The amplitude and mid-position of the cylinder oscillations

The variations of the amplitude and the mid-position of the cylinder oscillations with the angular position of the wire are shown in figures 8 and 9, respectively. In these figures, a polynomial curve is fitted for each range of wire angular positions to demonstrate the overall change. To fit the data within each range to a polynomial function, a standard least-squares algorithm is used. The order of the polynomial function is selected manually. In figure 8 and throughout the study, the amplitude of the cylinder oscillations is defined as half of the distance between the two overall phase-averaged limiting positions that the cylinder sweeps during its oscillations, as explained in § 2, and this amplitude is given in non-dimensionalized form based on the cylinder diameter  $D$ , as denoted by  $A^*$  (see (2.1)). The mid-position of the cylinder oscillation  $y_{mid}^*$  is calculated by averaging the displacement signal, and it is also normalized using the cylinder diameter ( $y_{mid}^* = y_{avg}/D$ ).

As can be seen in figure 8, as the wire angle increases within the angular range I ( $0^\circ \leq \theta < 47^\circ$ ), the oscillation amplitude  $A^*$  decreases, attaining its minimum value at  $\theta = 46^\circ$ , which is 37% lower than the amplitude of a clean (untripped) cylinder that undergoes VIV under the same flow conditions. Meanwhile, figure 9 depicts that, in this same range ( $0^\circ \leq \theta < 47^\circ$ ), the mid-position  $y_{mid}^*$  of oscillations increases significantly with the wire angle, which implies that the wire in this range induces a gradually increasing net time-averaged lift force towards the wire side of the cylinder as  $\theta$  increases. Remember that the range

## Effects of a single spanwise surface wire

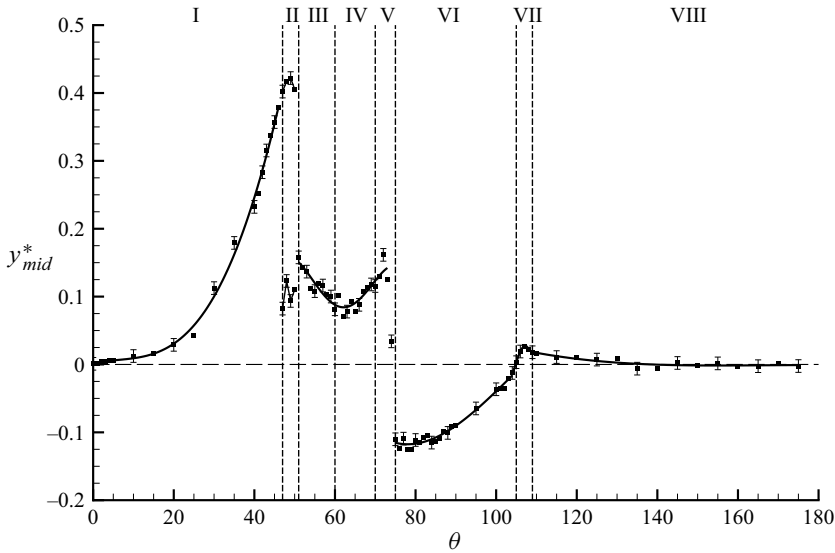


Figure 9. Variation of the mid-position  $y_{mid}^*$  of the oscillating cylinder with the wire angular position. The positive direction of the vertical axis corresponds to the wire side of the cylinder.  $y_{mid}^* = 0$  is the equilibrium state in still water for both clean and tripped cylinders. The horizontal dashed line indicates the mid-position of oscillation for the clean cylinder. The uncertainty is the same for all cases and is marked on the plot for some data points as a reference.

of the first critical angle for a stationary cylinder exposed to the same flow conditions was  $41.2^\circ \leq \theta_{c1} < 43^\circ$  (as discussed earlier in § 3.1), which falls within the range I of the cylinder undergoing VIV. As discussed earlier, this critical wire location was attributed to the attenuation of the Kármán instability, in the time-averaged sense, for stationary cylinders. However, the cylinder undergoing VIV motion here shows a regular sinusoidal motion at  $\theta_{c1}$ , similar to the results presented in figures 4–6, while its oscillation amplitude is decreased considerably compared with the clean cylinder undergoing VIV, as apparent in figure 8.

In angular range II ( $47^\circ \leq \theta < 51^\circ$ ), figure 8 shows a gradual increase in the amplitude of cylinder oscillations with increasing wire angle. As seen earlier in figure 4, the seemingly sinusoidal oscillation of the cylinder is intermittently disrupted by an irregular motion that involves a range of amplitudes from low to high. However, the high-amplitude irregular motion dwarfs the low-amplitude irregular motion, and that is the reason for the abrupt increase in the amplitude of the cylinder oscillations at the beginning of range II. Due to the presence of both somewhat sinusoidal and irregular motions in this range, two mid-positions can be defined for the cylinder oscillations, as seen in figure 9. The higher values in the mid-position  $y_{mid}^*$  plot of range II in figure 9 correspond to the near sinusoidal motion, while the lower data points in the same plot represent the mid-position of the oscillations during irregular motion. As the switch of the oscillations between the regular and irregular motions is intermittent for all  $\theta$  in this range, the cylinder oscillates sometimes around the upper and sometimes around the lower mid-position given in figure 9 for range II.

The overall inspection of figure 8 shows that, throughout the angular ranges II, III, IV and V, the oscillation amplitude of the cylinder continually increases with the wire angular position, reaching its highest value at  $\theta = 73^\circ$  (in the angular range V), which is 102 % higher than the oscillation amplitude of the clean cylinder. Note that attainment of such a

large level of oscillation amplitude at this  $\theta$  was observed to persist even for a wide range of  $U^*$  values (related result not shown here for brevity). Moreover, [figure 9](#) shows a gradual decrease of the mid-position of the cylinder oscillations with increasing wire angle in the angular range III, and an increase in ranges IV and V.

As seen earlier in [figures 4](#) and [5](#), both the pattern and the frequency of oscillations change abruptly at  $\theta = 75^\circ$  (which is the start of range VI). Likewise, at this  $\theta$ , abrupt changes are also visible in both the amplitude and the mid-position of the cylinder oscillations from [figures 8](#) and [9](#), respectively. In the angular range VI, [figure 8](#) depicts that the oscillation amplitude decreases with increasing wire angular position. Interestingly, the negative value of the cylinder mid-position in range VI (in [figure 9](#)) implies that the oscillating cylinder is pushed towards its clean side by the effect of the wire (unlike the other ranges). It should be noted that the range of the second critical angle for the stationary cylinder counterpart ( $50^\circ \leq \theta_{c2} \leq 80^\circ$ ) is a wide range, which starts from the end of range II and extends to the beginning of range VI of the wire-fitted cylinder undergoing VIV. As discussed earlier, the wire at  $\theta_{c2}$  enhances the Kármán vortex shedding from the stationary cylinder. However, the employment of the wire in the range of the second critical angle of the stationary cylinder has varying effects on the motion characteristics of the oscillating cylinder, depending on the  $\theta$  range defined in [figure 4](#).

In the angular range VII, the oscillation amplitude of the cylinder dropped drastically, with the wire at  $\theta = 107^\circ$  yielding the minimum value, which is 98% lower than the amplitude of the clean cylinder ([figure 8](#)). At and around  $\theta = 107^\circ$ , as seen earlier in [figure 4](#), the cylinder is almost motionless, and its mid-position stays near its equilibrium position, as shown in [figure 9](#). This level of amplitude attenuation was observed at around this  $\theta$  even over a wide range of reduced velocities. This observation is extremely significant and suggests that something as simple as a single spanwise wire can be used to suppress the VIV of a cylinder almost totally.

The sinusoidal oscillations for the cylinder resume starting from  $\theta = 109^\circ$  (which is the start of the angular range VIII). For the wire angular positions in range VIII, [figure 8](#) shows that the amplitude of oscillations increases with increasing  $\theta$ , approaching asymptotically a finite value of  $A^* = 0.61$ . Furthermore, inspection of [figure 9](#) shows that the cylinder oscillations in range VIII occur around its equilibrium position.

The characteristics of the cylinder motion discussed so far are expected to be intimately related to the vortex shedding mechanism. To elucidate this aspect, the subsequent section focuses on the flow field characteristics.

### 3.4. Flow field characteristics

#### 3.4.1. Near-wake structure

In this section, to increase insight into the vortex shedding patterns associated with different wire locations, contour patterns of instantaneous vorticity in the near-wake region will be discussed in relation to the cylinder motion for all wire angular ranges. The results presented here aim to reveal the vortex shedding processes featured by the different wire angular ranges, and during this investigation, no assumption is made regarding the phase difference between the fluid forcing and the cylinder motion. In all figures given here, the flow is from left to right, and the wire (not shown in the figures) is located on the upper side of the image of the cylinder. On the contour plots of the instantaneous vorticity, an arrow shown on the image of the cylinder signifies the direction of the cylinder motion at that instant. No arrow is provided whenever the cylinder comes to an instantaneous stop at the beginning or end of an oscillation stroke. Also, in the figures, the time is represented

in non-dimensional form  $t^* = tU/D$  and its origin is selected to be the instant when the cylinder is at its lowest point in the particular cycle that is being discussed.

In [figure 10](#), the contours of instantaneous non-dimensional vorticity  $\omega D/U$  are shown for the wire at  $\theta = 45^\circ$  at instants corresponding to four different cylinder positions selected from one full oscillation cycle of the cylinder. These four cylinder positions are marked on the time trace of the cylinder position, which is also given in the same figure. The wire position  $\theta = 45^\circ$  belongs to angular range I. Inspection of the contour plots in [figure 10](#) reveals the following vortex shedding process at this  $\theta$ : when the cylinder is at position 1 (marked on the  $y^*$  versus  $t^*$  plot), a vortex indicated as  $V_1$  is formed near the upper side (wire side) of the cylinder. This vortex grows in size and is shed further downstream when the cylinder is at the mid-position of the cycle (position 2). Then, when the cylinder is at its top-most position in this cycle (position 3), another vortex, named  $V_2$ , is formed.  $V_2$  is significantly stretched and shed in the downstream direction while also moving in the transverse direction when the cylinder reaches position 4, which is a position that comes slightly after the mid-position of this oscillation cycle during the downward stroke. The characteristics of  $V_1$  and  $V_2$  are different;  $V_1$ , on the wire side, has a nearly circular shape and travels along the streamwise direction while  $V_2$  stretches and moves in the transverse direction (in the positive  $y^*$  direction) as it sheds downstream. The observed process of vortex shedding for  $\theta = 45^\circ$  may be considered, at first sight, to be similar to the 2S vortex shedding mode, which was revealed by Williamson & Roshko (1988) for clean cylinders undergoing VIV at low reduced velocities. As discussed in their study, in the 2S vortex shedding mode, one vortex is shed during the acceleration of the cylinder at each half of the oscillation cycle, and vortices travel in the streamwise direction in a row. However, in the present case, although there is one single vortex shed per half-cycle, the character of the second vortex is very different from the 2S mode. The second vortex shedding from the smooth side undergoes significant stretching and lateral movement while convecting downstream, which is presumably why the cylinder has been pushed toward the wire side so significantly, as seen in [figure 9](#).

When the wire is placed at the angular positions of range II, starting from  $\theta = 47^\circ$ , the sinusoidal motion of the cylinder is intermittently disrupted, as demonstrated earlier in [figure 4](#) for a representative  $\theta$  from this range. [Figure 11](#) shows the normalized vorticity contours at four instants selected from different parts of the cylinder's motion for  $\theta = 48^\circ$  as an example case from range II. Points 1 and 2, marked on the  $y^*$  versus  $t^*$  plot, are instants from a cycle during the cylinder's sinusoidal motion. Point 1 shows the instant when the cylinder is moving away from its lowest point. This point comes slightly after the start of this upward move. Point 2 is  $\pi$  away from point 1 in the cycle and corresponds to an instant when the cylinder is moving away from its top-most position. As the cylinder passes from points 1 and 2, vortices  $V_1$  and  $V_2$  are formed, respectively, and the vortex shedding process appears to be generally the same as that observed for range I. In this case also  $V_2$  is stretched and moves in the transverse direction as the cylinder passes the mid-position of the cycle in its downward stroke (which is not shown in [figure 11](#) for brevity). Point 3 is from an instant when the wire interrupts the vortex shedding and introduces irregular cylinder motion. At this point, there are two streams of vorticity coming from each side of the cylinder. Later on, the regular Kármán vortex shedding resumes, as is the case at point 4, creating a new vortex, marked as  $V'_1$ , which yields sinusoidal cylinder motion again. From these results, it can be concluded that, in range II, the cylinder switches intermittently between two modes of oscillation (i.e. sinusoidal and irregular motions), which is accompanied by a corresponding switch in the vortex shedding process.

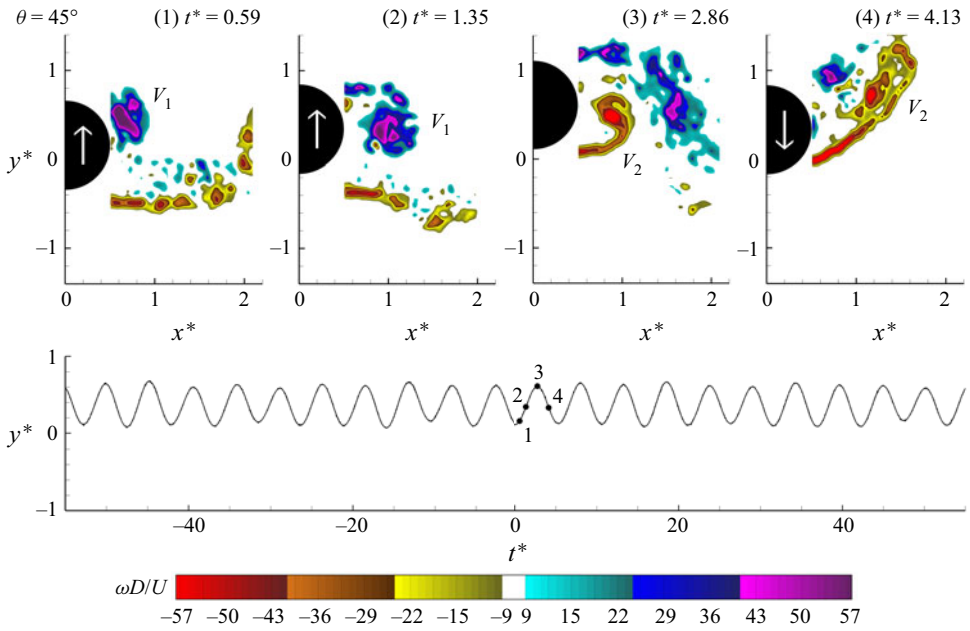


Figure 10. Contours of instantaneous normalized vorticity ( $\omega D/U$ ) for the wire angular position  $\theta = 45^\circ$  (from range I) along with the time traces of the cylinder displacement. The minimum absolute value and the incremental value of contour levels are:  $[|\omega|D/U]_{min} = 9$  and  $\Delta(\omega D/U) = 1.15$ .

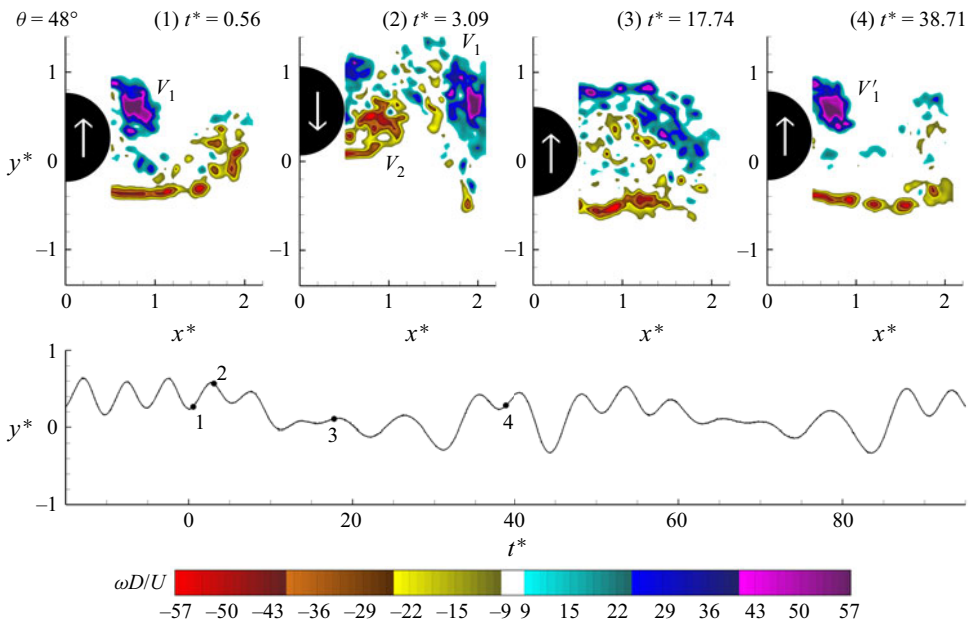


Figure 11. Contours of instantaneous normalized vorticity ( $\omega D/U$ ) for the wire angular position  $\theta = 48^\circ$  (from range II) along with the time traces of the cylinder displacement. The minimum absolute value and the incremental value of contour levels are:  $[|\omega|D/U]_{min} = 9$  and  $\Delta(\omega D/U) = 1.15$ .

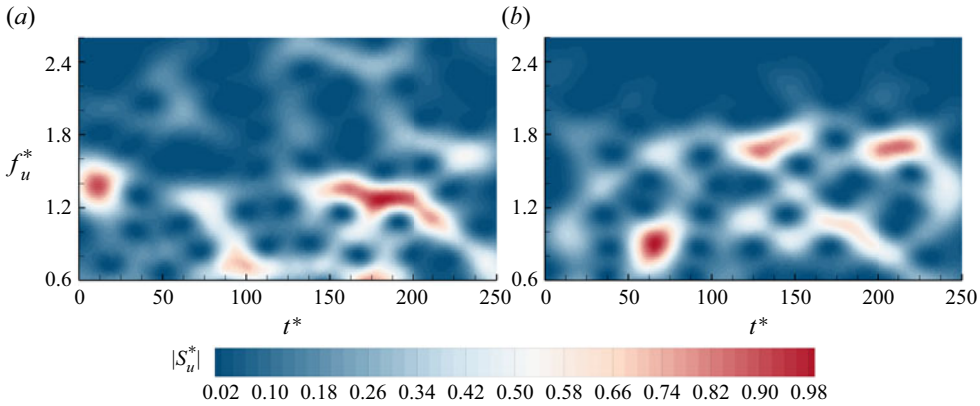


Figure 12. Time–frequency spectrogram of the streamwise velocity component for: (a) the stationary cylinder with the wire at the first critical angle ( $\theta_{c1} = 42^\circ$ ), and (b) the oscillating cylinder with the wire placed at  $\theta = 48^\circ$  (within the angular range II). The magnitude of spectra  $|S_u^*|$  is normalized based on the maximum value in the entire period, and the incremental value of the contour levels is  $\Delta[|S_u^*|] = 0.02$ .

The switch in the vortex shedding mode of the oscillating wire-fitted cylinder for the angular range II ( $47^\circ \leq \theta < 51^\circ$ ) is remarkably similar to the switch between the irregular shedding and the regular shedding modes first observed by Aydin *et al.* (2014) for a stationary cylinder when the wire is at a first critical angle. Recall from § 3.1 that the range of the first critical angle for the stationary cylinder was found to be  $41.2 \leq \theta_{c1} < 43^\circ$  for the wire size and Reynolds number considered in the present study. In the referenced work of Aydin *et al.* (2014), it was shown that for the stationary cylinder, the wire at  $\theta_{c1}$  causes the formation of Kármán vortices to stop for the majority of the time, while the regular vortex shedding resumes only intermittently for short periods of time. For the oscillating cylinder in the present work, the wire at angular range II induces irregularities in the cylinder motion at a wide range of frequencies, as shown in figure 7, and the regular vortex shedding occurs intermittently, as seen in figure 11. To further investigate the similarity in vortex shedding interruption between the stationary and oscillating wire-fitted cylinders, the streamwise velocity signal  $u$  was extracted from the PIV data at point  $(1.35D, 0.56D)$  in the near wake and the corresponding time–frequency spectrogram was obtained from the STFT analysis. The contour plots in figure 12 show these spectrograms for the stationary cylinder fitted with the wire at the first critical angle  $\theta_{c1} = 42^\circ$  and the oscillating cylinder fitted with the wire at  $\theta = 48^\circ$ . These plots depict the variation of the normalized frequency of the streamwise velocity ( $f_u^* = f_u/f_n$ ) with the non-dimensional time ( $t^* = tU/D$ ). At times when there is a regular vortex shedding, a specific dominant frequency for flow fluctuations is visible from the high-amplitude contour levels in figure 12. From these spectrograms, it is clear that the vortex shedding process is sporadic for both the stationary and oscillating wire-fitted cylinders in question. Hence, it can be concluded that, for the oscillating cylinder, the effect of wire on disrupting the vortex shedding is shifted to the angular positions of range II ( $47^\circ \leq \theta < 51^\circ$ ), which are higher than the first critical angles of the stationary cylinder ( $41.2^\circ \leq \theta_{c1} < 43^\circ$ ).

In the wire angular range III, it has been seen so far that the cylinder motion is the superposition of two sinusoidal oscillations with different frequencies (as discussed in figures 5–8). This observation can be linked to the vortex shedding process, which is depicted in figure 13 for the representative  $\theta = 53^\circ$  case from range III. When the cylinder starts its upward motion in the positive  $y^*$  direction (at position 1), a vortex indicated as

$V_1$  forms. This vortex sheds when the cylinder reaches the mid-position of the cycle (the corresponding vorticity contour is not shown in the figure). Another vortex,  $V_2$ , forms as the cylinder continues to move upwards toward position 2, and this vortex sheds when the cylinder is at the top position of the oscillation pattern. During the acceleration of the cylinder in the negative  $y^*$  direction, a third vortex,  $V_3$ , forms near the wire side of the cylinder ( $V_3$  formation during downward stroke is not shown in the figure). In this case, the wire has induced an additional vortical structure, and the cylinder gains an additional reciprocal motion. As can be seen from the time trace of the cylinder position given in [figure 13](#), for position 3, the cylinder motion diverges starting near the mid-position of the downward stroke of the first sinusoidal motion and  $V_3$  has already shed when the cylinder starts to move in this positive  $y^*$  direction. Next,  $V_4$  is formed from the clean side of the cylinder as the cylinder moves in the negative  $y^*$  direction. Consequently, four vortices are shed per cycle for wire angular range III. This vortex pattern is different from the 2P vortex shedding mode observed during the VIV of a clean cylinder in the lower synchronization range. In the 2P mode, as Williamson & Roshko (1988) discussed, two vortices are shed per half-cycle, and two vortices of opposite sign pair together while travelling downstream. In the vortex pattern of  $\theta = 53^\circ$  (representative of range III) given in [figure 13](#), four vortices are shed in total; however, they do not travel together. It is worth mentioning here that, for higher angles in range II, when the cylinder oscillation pattern switches between being sinusoidal and irregular, the vortex shedding mode just discussed for range III is observed occasionally, and as a result, the vortex shedding mode alternates between three modes: the mode observed for range I, the mode observed for range III and the no regular vortex shedding mode (the corresponding results are not shown here for brevity). This switch in the vortex modes in range II is irregular, resulting in a change in the oscillation pattern as the wire angular location increases toward range III.

The wire at angular locations of range IV induces quasi-sinusoidal oscillations with the random appearance of irregular motions, as can be seen in the time trace of the displacement signal given in [figure 14](#) for  $\theta = 60^\circ$  as a representative case from this range. [Figure 14](#) also shows the vortex shedding process for this  $\theta$  over two consecutive oscillation cycles. The first oscillation cycle of the cylinder motion that includes positions 1 to 4 is similar to the oscillation motion observed in range III. Accordingly, the vortex shedding process in the first cycle shown in [figure 14](#) for range IV is also identical to the vortex shedding process of range III. As described earlier for [figure 13](#), four vortices are shed in one cycle, and the last two vortices (marked as  $V_3$  and  $V_4$  in the vorticity contour plots of positions 3 and 4 in [figure 14](#)) induce an additional reciprocating motion on the oscillating cylinder. However, the same vortex shedding process does not always yield this additional reciprocating motion, as seen in the second cycle, which includes positions 5 to 8 in [figure 14](#). At position 5, the first vortex of the cycle, indicated as  $V'_1$ , is formed. This vortex moves downstream as the cylinder reaches the end of that upward stroke. The second vortex  $V'_2$  is formed and starts moving downstream as the cylinder changes its direction of motion right before position 6. At position 6, the cylinder moves slowly in the negative  $y^*$  direction. Then, the third vortex  $V'_3$  is shed at position 7. As the cylinder accelerates in the same direction toward position 8, the fourth vortex  $V'_4$  is forming. As can be seen in [figure 14](#), the vortex shedding processes of the second cycle and the first cycle are similar, while the motion of the oscillating cylinder is different. By comparing positions 3 and 7, it is visible that the two vortices,  $V_3$  and  $V'_3$ , look identical, but the direction of motion for the cylinder is opposite. It should be noted that this observed vortex

*Effects of a single spanwise surface wire*

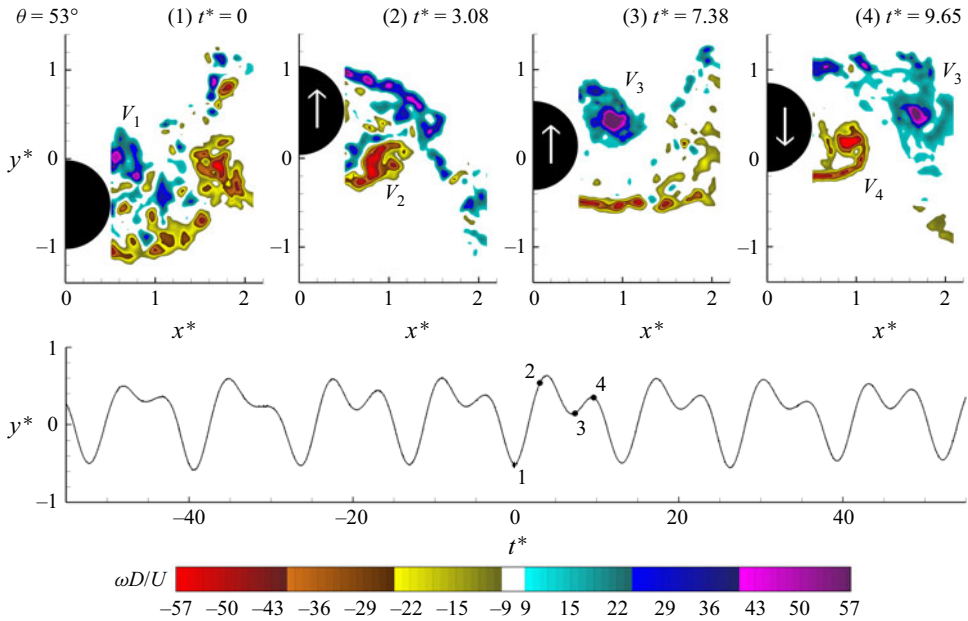


Figure 13. Contours of instantaneous normalized vorticity ( $\omega D/U$ ) for the wire angular position  $\theta = 53^\circ$  (from range III) along with the time traces of the cylinder displacement. The minimum absolute value and the incremental value of contour levels are:  $[|\omega|D/U]_{min} = 9$  and  $\Delta(\omega D/U) = 1.15$ .

shedding process is repeated in the rest of the oscillation pattern for  $\theta = 60^\circ$  as well as at all other angular locations in range IV.

In figure 15, the contours of instantaneous normalized vorticity are shown for  $\theta = 74^\circ$  as an example case from the wire angular range V. In this  $\theta$  range, the cylinder undergoes high-amplitude, nearly sinusoidal oscillations with one dominant frequency. However, the vortex shedding mechanism in range V is significantly different from the other ranges that exhibit sinusoidal cylinder motion. The vortex shedding process in range V appears to be similar to that in ranges III and IV. As the cylinder moves upward (in the positive  $y^*$  direction), a vortex, marked as  $V_1$  at position 1 in figure 15, forms from the upper side (which is the wire side) of the cylinder. At this position, the vortex marked as  $V_0$  is from the previous cycle. As the cylinder accelerates to the mid-position of the cycle,  $V_1$  stretches and moves laterally in the negative  $y^*$  direction. At position 2, the second vortex  $V_2$  is formed from the clean side of the cylinder. This vortex is moved to a downstream location at position 3. When the cylinder reaches the top-most position in the cycle, the wire induces the third vortex,  $V_3$ , which is seen at position 3;  $V_3$  travels downstream as the cylinder moves downward (in the negative  $y^*$  direction), as shown in position 4. Furthermore, the fourth vortex  $V_4$  is formed while the cylinder continues moving downward, as seen at position 4.  $V_4$  starts to travel downstream when the cylinder reaches the end of the cycle (not shown in the figure). In figure 15,  $V_4$  at position 4 is equivalent to  $V_0$  at position 1. Accordingly, for the wire angular range V, four vortices are shed per cycle, similar to the ranges III and IV; however, the cylinder motion is different, such that, in range V, the cylinder's direction of motion does not change when the additional vortex ( $V_3$ ) is induced, but when  $V_3$  is formed, the cylinder moves more slowly around the top position compared with a sinusoidal motion. A careful inspection of the cylinder oscillation pattern, given in figure 15, shows that the sinusoidal oscillation pattern is

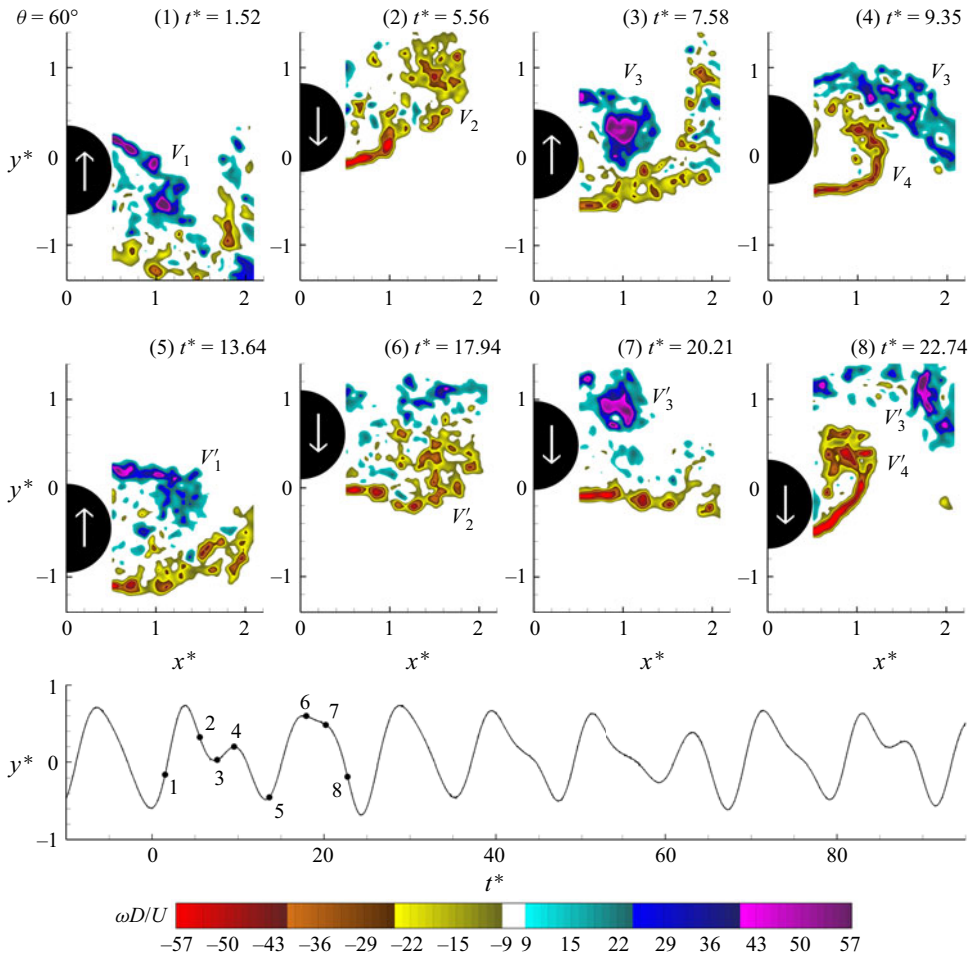


Figure 14. Contours of instantaneous normalized vorticity ( $\omega D/U$ ) for the wire angular position  $\theta = 60^\circ$  (from range IV) along with the time traces of the cylinder displacement. The minimum absolute value and the incremental value of contour levels are:  $[|\omega|D/U]_{min} = 9$  and  $\Delta(\omega D/U) = 1.15$ .

not symmetrical. The peaks are wider than the valleys. Although four vortices are shed per cycle for the wire angular range V, the vortex shedding pattern cannot be confirmed as the 2P vortex shedding mode of a clean cylinder because the pairing of vortices in the downstream region of the wake is not visible from the current field of view. On rare occasions, the vortex shedding process in range V is interrupted (not shown in the figure), which causes a temporary drop in the amplitude of the cylinder oscillation accompanied by a short-time small increase in the oscillation frequency; one such instance was seen in the time–frequency spectrogram of  $\theta = 72^\circ$  (from range V) in figure 6.

The subsequent wire angular range is range VI, for which the cylinder depicts a quasi-sinusoidal motion with a lower amplitude and higher frequency in comparison with range V. Range VI starts at  $\theta = 75^\circ$ , for which the cylinder oscillation pattern and the vorticity contours are presented in figure 16. Similar to the sinusoidal oscillation pattern of range I, two vortices are shed for the wire angular positions within range VI. The first vortex,  $V_1$  on the wire side, is forming at position 1 (which corresponds to the phase when the cylinder starts to accelerate upwards). At position 2,  $V_1$  is seen at a

## Effects of a single spanwise surface wire

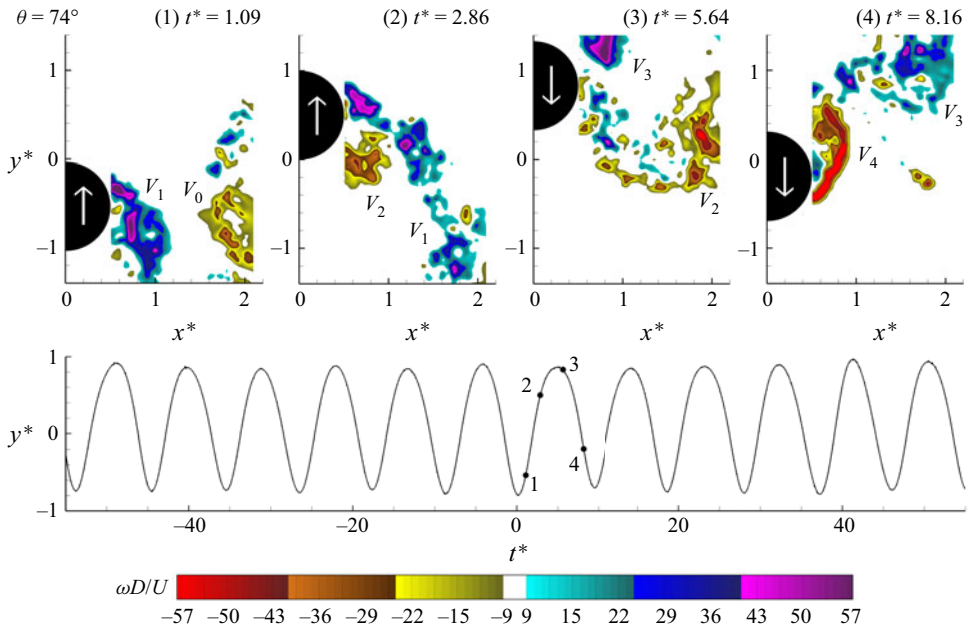


Figure 15. Contours of instantaneous normalized vorticity ( $\omega D/U$ ) for the wire angular position  $\theta = 74^\circ$  (from range V) along with the time traces of the cylinder displacement. The minimum absolute value and the incremental value of contour levels are:  $[|\omega|D/U]_{min} = 9$  and  $\Delta(\omega D/U) = 1.15$ .

downstream location. Next, the second vortex  $V_2$  is formed from the clean side of the cylinder, as seen at position 3;  $V_2$  is shedding downstream when the cylinder passes the mid-position of the cycle at position 4. The characteristics of vortices in range VI are different from the previous ranges, such that the vortices are more stretched and the small-scale structures are more discernible in the vorticity contours.

When the wire is placed in the  $\theta$  range VII ( $105^\circ \leq \theta < 109^\circ$ ), figure 4 revealed that the sinusoidal oscillation motion of the cylinder ceases, and figure 8 depicted that the amplitude of the cylinder motion reduces by more than 90% compared with the clean cylinder case. Contour patterns of instantaneous normalized vorticity ( $\omega D/U$ ) are shown in figure 17 for the cylinder that is fitted with the wire at  $\theta = 107^\circ$ , which is the case yielding the largest-amplitude reduction in cylinder motion (to be specific, 98% reduction compared with the clean cylinder). Note that, for the wire angular range VII, experiments were repeated with an extended field of view in the downstream direction to better investigate the observed vortex shedding modes. Two distinct vortex shedding modes are revealed in this range. Figure 17(a) depicts a snapshot from one of these modes, named Mode I here. In this mode, vortices are shed alternately into the wake. Moreover, in this mode, the vortices do not move away from the cylinder centreline as they convect downstream. The second mode, Mode II, is depicted as a snapshot in figure 17(b). In this mode, two vortices that are symmetric about the cylinder centreline form (marked as  $V'_1$  and  $V'_2$ ). After circulating in their position for a brief while, they shed downstream in the form of small-scale vortices along the centreline of the cylinder. Long-time PIV records of the near wake (for approximately 54 vortex shedding cycles) show that the vortex shedding pattern switches randomly between these two vortex shedding modes (Mode I and Mode II).

To further assess the random switch between the two vortex shedding modes (Mode I and Mode II), STFT of the streamwise velocity signal,  $u$ , extracted from one point in

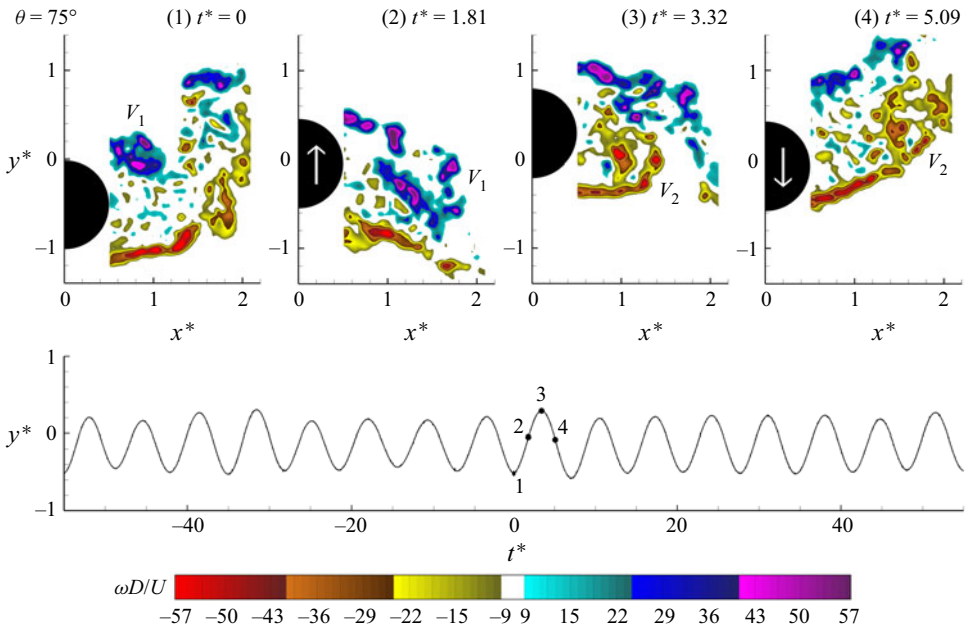


Figure 16. Contours of instantaneous normalized vorticity ( $\omega D/U$ ) for the wire angular position  $\theta = 75^\circ$  (from range VI) along with the time traces of the cylinder displacement. The minimum absolute value and the incremental value of contour levels are:  $[|\omega D/U]_{min} = 9$  and  $\Delta(\omega D/U) = 1.15$ .

the near wake of the clean cylinder undergoing VIV motion is compared with that of a cylinder fitted with the wire at  $\theta = 107^\circ$ . The STFT of the streamwise velocity signal is calculated at point  $(1.62D, 0.51D)$  for the clean cylinder and at point  $(2.13D, -0.41D)$  for the cylinder having the wire at  $\theta = 107^\circ$  to represent the differences discernibly. Figure 18 shows the variation of the spectral amplitude, which is normalized by its maximum value in the entire time period studied. The clean cylinder oscillates with a constant frequency, and its synchronized vortex shedding frequency has a fixed frequency of  $f_u^* = 1.31$ , as apparent from figure 18(a). For the same flow conditions, when the wire is paced at  $\theta = 107^\circ$ , the vortex shedding frequency varies, as shown in figure 18(b). The high spectral amplitudes (coloured in red based on the colour bar) correspond to the instants where the alternating shedding of vortices occurs (Mode I), and the lower magnitudes of spectra point out to the periods of interrupted vortex shedding (Mode II). Note that Mode I involves the shedding of vortices at a frequency identical to the vortex shedding frequency of a stationary clean cylinder at  $Re = 10^4$  ( $f_u^* = 2.14$ , or in other words,  $St = 0.21$ ), while Mode II involves shedding of vortices with no predominant frequency. Although here the vortex shedding modes are depicted only for the  $\theta = 107^\circ$  case, these modes were equally observed for all  $\theta$  in range VII ( $105^\circ \leq \theta < 109^\circ$ ). It can be concluded that, in range VII, the wire achieves attenuation in the VIV response of the cylinder by altering the shedding mode of the vortices.

In range VIII, the cylinder resumes its regular sinusoidal oscillation motion with one dominant frequency, as discussed in figures 4 and 5. The vortex shedding process for  $\theta = 140^\circ$  as a representative of range VIII is shown in figure 19, along with the time trace of the cylinder oscillation. The vortex shedding in this range of wire angular locations involves four vortices. When the cylinder is accelerating at the beginning of the cycle in the positive  $y^*$  direction, the first vortex  $V_1$  is formed. This vortex is moved downstream

Effects of a single spanwise surface wire

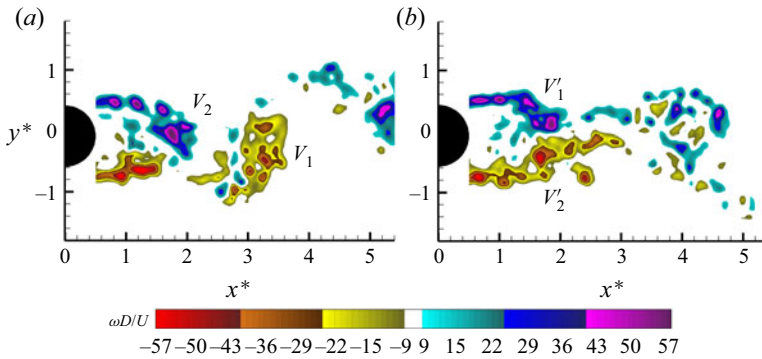


Figure 17. Contours of instantaneous normalized vorticity ( $\omega D/U$ ) for the wire angular position  $\theta = 107^\circ$  (from range VII) with random switching of the vortex shedding mode between (a) Mode I and (b) Mode II. The minimum absolute value and the incremental value of contour levels are:  $[|\omega|D/U]_{min} = 9$  and  $\Delta(\omega D/U) = 1.15$ .

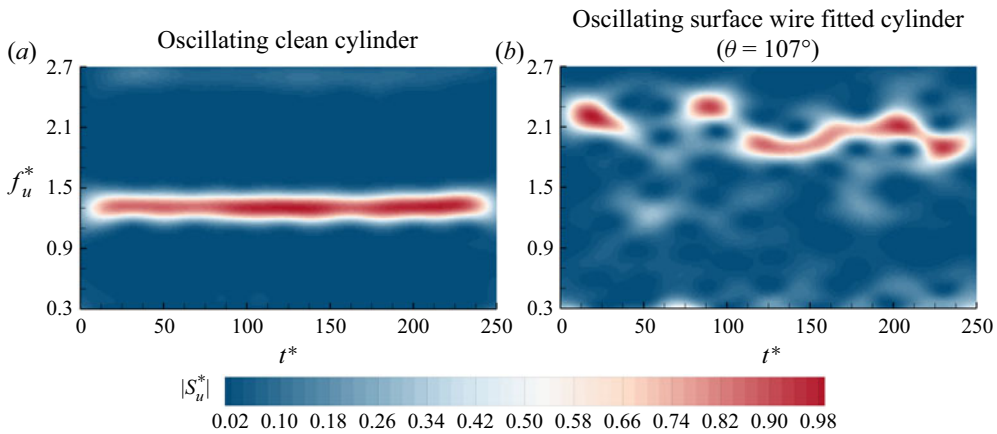


Figure 18. The short-time Fourier transform (STFT) of the streamwise velocity for: (a) the clean cylinder and (b) the cylinder fitted with the wire at  $\theta = 107^\circ$ . The magnitude of the velocity spectra is normalized based on the maximum value in the entire period. The normalized frequency resolution is 0.02 and the temporal resolution is 0.21 s. The incremental value of contour levels is  $\Delta[|S_u^*|] = 0.02$ .

at position 1. When the cylinder passes the mid-position of the cycle, the second vortex  $V_2$  with the same vorticity sign as  $V_1$  is shed, which can be seen at a downstream location later at position 2. During the second half of the cycle, the third vortex  $V_3$  forms from the smooth side of the cylinder. This vortex is seen at a downstream location at position 3. The fourth vortex  $V_4$  with the same vorticity sign as  $V_3$  starts to form slightly after the mid-position of the cycle. In figure 19,  $V_4$  is seen at a downstream location at position 4 (when the cylinder reaches the end of the cycle). Based on these results, it can be concluded that four vortices are shed in a given oscillation cycle of the wire-fitted cylinder for the wire angular locations of range VIII, and during this shedding process, two vortices of the same vorticity sign (e.g.  $V_1$  and  $V_2$ ) shed one after another. This vortex shedding process is remarkably similar to the 2P vortex shedding mode reported by previous studies for clean cylinders oscillating within the lower synchronization range (Brika & Laneville 1993; Govardhan & Williamson 2000). This similarity between the clean cylinder and the cylinder with the wire attached at the angular locations of range VIII was further verified in the present study by examining the vortex shedding from the clean cylinder

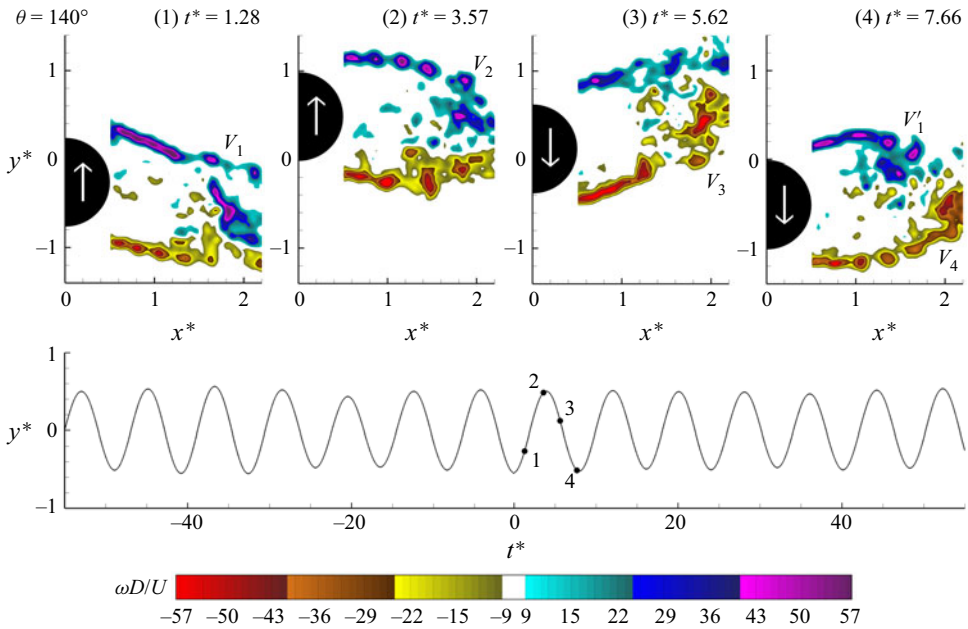


Figure 19. Contours of instantaneous normalized vorticity ( $\omega D/U$ ) for the wire angular position  $\theta = 140^\circ$  (from range VIII) along with the time traces of the cylinder displacement. The minimum absolute value and the incremental value of contour levels are:  $[\omega D/U]_{min} = 9$  and  $\Delta(\omega D/U) = 1.15$ .

undergoing VIV under the same conditions. The results of the oscillating clean cylinder are not presented here for brevity.

### 3.4.2. Global patterns of velocity spectra

To gain further insight into the unsteady flow characteristics, global representations of velocity spectra have been constructed from the PIV data. This process involved the determination of the autospectra of the streamwise velocity fluctuations at every point in the PIV field of view, detection of the frequency of streamwise velocity fluctuations prevailing over the entire flow field and plotting of the spectral amplitude corresponding to this frequency over the entire near-wake region in the form of contour plots. The contour plots presented in figure 20 show the amplitude of the streamwise velocity spectra,  $|S_u(f_u^*)|$ , at the prevailing frequency of streamwise velocity fluctuations. In this figure, the plots are provided for select wire positions representative of each angular range. The prevailing frequency of velocity fluctuations depends on the wire location  $\theta$ , and its value is indicated for each  $\theta$  in figure 20 in non-dimensional form  $f_u^*$  (based on the natural frequency of the system, i.e.  $f_u^* = f_u/f_n$ ). Also, to take into account the global effect of the cylinder motion on the near-wake flow field, the mid-position and the oscillation amplitude  $A^*$  are also marked in figure 20 on the images of the cylinder. The wire (not shown in the figure) is positioned on the upper side of the cylinder in these plots.

The most salient observation that comes out of the overall inspection of the plots in figure 20 is that, for both wire angular positions of  $\theta = 48^\circ$  (from range II) and  $\theta = 107^\circ$  (from range VII), the peak spectral amplitudes are relatively low over the whole near-wake region in comparison with the peak spectral amplitudes of the other angular positions. This attenuation is observed not only for the representative  $\theta$  given from the angular ranges II and VII, but also for all wire placement angles of these two ranges. As a result,

## Effects of a single spanwise surface wire

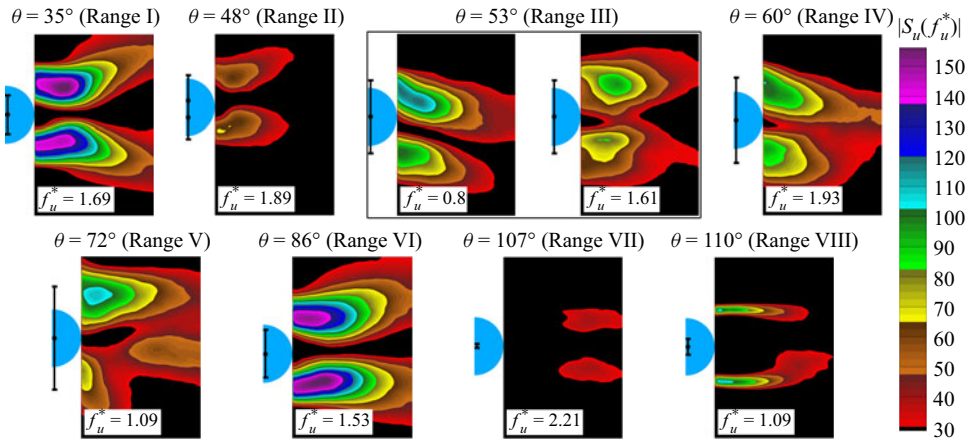


Figure 20. Contours of the amplitude of the autospectral density corresponding to the streamwise velocity component at the prevailing frequency of velocity fluctuations  $|S_u(f_u^*)|$  for different wire angular positions that are representative of each wire angular range. The mid-position and the displacement range of the cylinder are also depicted on the image of the cylinder in each plot. Minimum and incremental values are as follows:  $[|S_u(f_u^*)|]_{min} = 30 \text{ mm s}^{-1}$  and  $\Delta[|S_u(f_u^*)|] = 2.5 \text{ mm s}^{-1}$ .

no prominent frequency was detectable for the angular ranges II and VII. The spectral amplitudes in the contour plots of  $\theta = 48^\circ$  and  $\theta = 107^\circ$  in figure 20 correspond to an arbitrarily selected frequency; however, the same low-amplitude contours existed for all other frequencies at these angles. For the angular ranges II and VII, the non-existence of a dominant frequency corresponding to velocity fluctuations in the wake implies that the strength and coherence of Kármán vortices (indicated by the magnitude of the autospectral density) are drastically attenuated for these wire positions. Notice that this attenuation is more significant in range VII compared with range II because of the observed random switch between the vortex shedding Modes I and II.

For all wire angular positions outside the angular ranges II and VII, a dominant frequency was distinctively identifiable from the spectra of the streamwise velocity component. The peak amplitudes of velocity spectra can ultimately be related to the coherence and strength of periodic vortex shedding. For wire applications that lead to regular sinusoidal motion, such as those within the angular ranges I, V, VI and VIII, very high peak amplitudes are visible in the contour plots of  $|S_u(f_u^*)|$  in figure 20, indicating highly coherent shedding of vortices. For the wire angular range IV, it was deduced from the time traces of the cylinder motion, given in figure 4, as well as the time–frequency spectrogram of cylinder oscillations, given in figure 6, that the sinusoidal cylinder motion is disturbed intermittently by irregular oscillations. The lower spectral peak observed in velocity fluctuations in figure 20 for the representative case of  $\theta = 60^\circ$  from this range compared with the above-mentioned ranges (I, V, VI and VIII) is consistent with the intermittently appearing irregular cylinder motion, pointing out the intimate link between unsteady flow characteristics and the cylinder motion.

The two frequencies dominating the cylinder oscillation motion simultaneously, detected earlier in figure 5, for the wire locations in range III are also the predominant frequencies in the streamwise velocity spectra. Therefore, for the representative case of  $\theta = 53^\circ$  in figure 20, two autospectral density contours are provided corresponding to these two frequencies dominating the velocity fluctuations. The peak spectral amplitudes detected in these two plots have comparable levels. However, the locations of these peaks

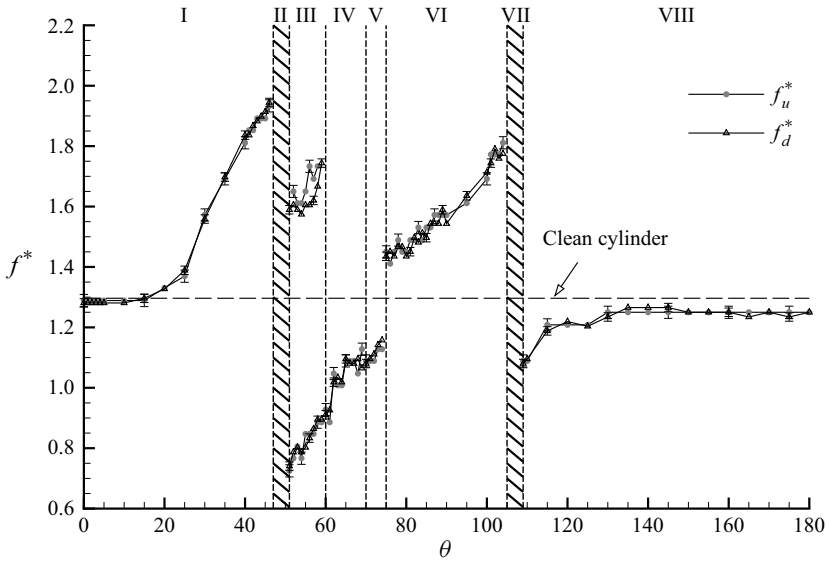


Figure 21. Variation of the dominant frequency of the oscillation motion  $f_d^*$  and the dominant frequency of the streamwise velocity fluctuations  $f_u^*$  with the wire angular position  $\theta$  for the oscillating wire-fitted cylinder. The horizontal dashed line marks both the oscillation frequency and the dominant frequency of streamwise velocity signals for the clean cylinder undergoing VIV under the same conditions.

in the near wake are relatively upstream for the lower dominant frequency, reasons of which are not immediately apparent.

### 3.4.3. Vortex shedding synchronization

Figure 21 depicts the dominant non-dimensional vortex shedding frequency based on the streamwise velocity component ( $f_u^* = f_u/f_n$ ) as a function of the wire angular position. For determining the dominant vortex shedding frequency, the global autospectral density of the streamwise velocity signals, obtained from the PIV data, was calculated for a wide range of frequency values, and the frequency with the highest peak magnitude of spectra from the near wake was selected as the dominant frequency. The non-dimensional oscillation frequency of the cylinder ( $f_d^* = f_d/f_n$ ) from figure 5 is also shown in this figure for comparison. For the clean cylinder counterpart, it is known that the vortex shedding is synchronized with the oscillation motion as the reduced velocity considered in the present study ( $U^* = 10.44$ ) is from the lower synchronization range, as discussed earlier in § 3.2. Hence, for the clean cylinder  $f_u^* = f_d^*$ . The horizontal line in figure 21 marks the dominant non-dimensional frequency of both the cylinder oscillations and vortex shedding for the clean cylinder.

As can be seen from figure 21, similar to the case of the clean cylinder, the vortex shedding of the wire-fitted cylinder is synchronized with the oscillation motion of the cylinder for all angular positions of the wire, except for the angular ranges II ( $47^\circ \leq \theta < 51^\circ$ ) and VII ( $105^\circ \leq \theta < 109^\circ$ ). Hence, the ranges II and VII are hatched in figure 21. It should also be noted that, similar to figure 5, the interpretation of the hatched areas in figure 21 is different for the angular range II and range VII. In range II, the vortex shedding occurs intermittently (as shown in figure 11), and consequently, the cylinder randomly oscillates with sinusoidal and disturbed motions, as seen in figure 4. However, a dominant frequency cannot be selected for the entire period of the cylinder oscillation.

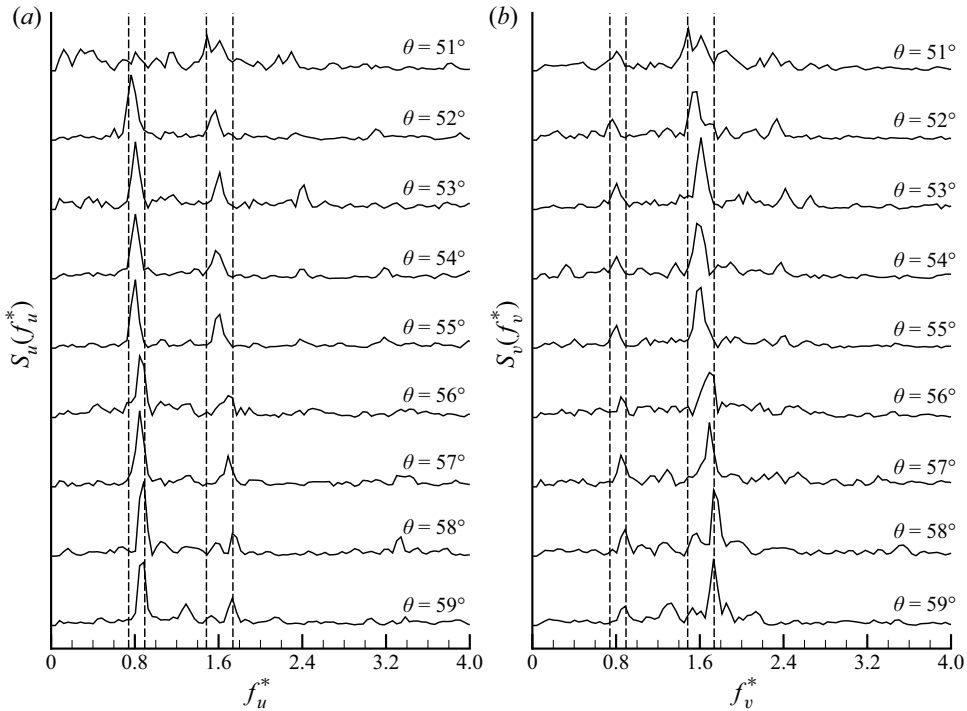


Figure 22. Frequency spectrum of velocity signals at a point with maximum value of spectral magnitude for wire angular positions of range III ( $51^\circ \leq \theta < 60^\circ$ ). Existence of two distinct dominant frequencies is depicted for both: (a) the streamwise velocity component  $u$  and (b) the transverse velocity component  $v$ .

On the contrary, in range VII, there is no detectable oscillation motion for the cylinder, and the vortex shedding switches intermittently between Mode I and Mode II (as shown in figure 17). As a result, there is no dominant frequency in range VII.

Another phenomenon revealed in figure 21 is the simultaneous presence of two dominant frequencies throughout the angular range III ( $51^\circ \leq \theta < 60^\circ$ ) not only for the cylinder oscillation motion but also for the vortex shedding process. The oscillation of the wire-fitted cylinder in range III was seen earlier (in figures 4–7) to be dominated by two sinusoidal motions having different frequencies. To demonstrate the existence of dual-frequency domination in velocity fluctuations for this angular range, figure 22 is provided, where the autospectral density of the streamwise  $u$  and transverse  $v$  components of the velocity,  $S_u(f_u^*)$  and  $S_v(f_v^*)$ , are shown for the wire angular positions of  $\theta = 51^\circ$  to  $59^\circ$  (angular range III). Each spectrum shown in figure 22 is determined using the velocity signal extracted from the PIV data corresponding to the respective point in the near wake that gives the highest spectral magnitude. As seen in figure 22(a), two distinct peaks are detectable in the spectra of the streamwise velocity component,  $S_u(f_u^*)$ . The first peak is always the predominant one for all wire angular positions, except for  $\theta = 51^\circ$ , which is the beginning of range III. On the other hand, figure 22(b) shows that the second peak is the predominant one in the spectra of the transverse velocity component,  $S_v(f_v^*)$ , for all angular locations in this range. In figure 22, the vertical dashed lines indicate the range of values within which the two dominant frequencies change with the wire angular location,  $\theta$ . The range of increase in the two dominant frequencies with increasing  $\theta$  is identical for

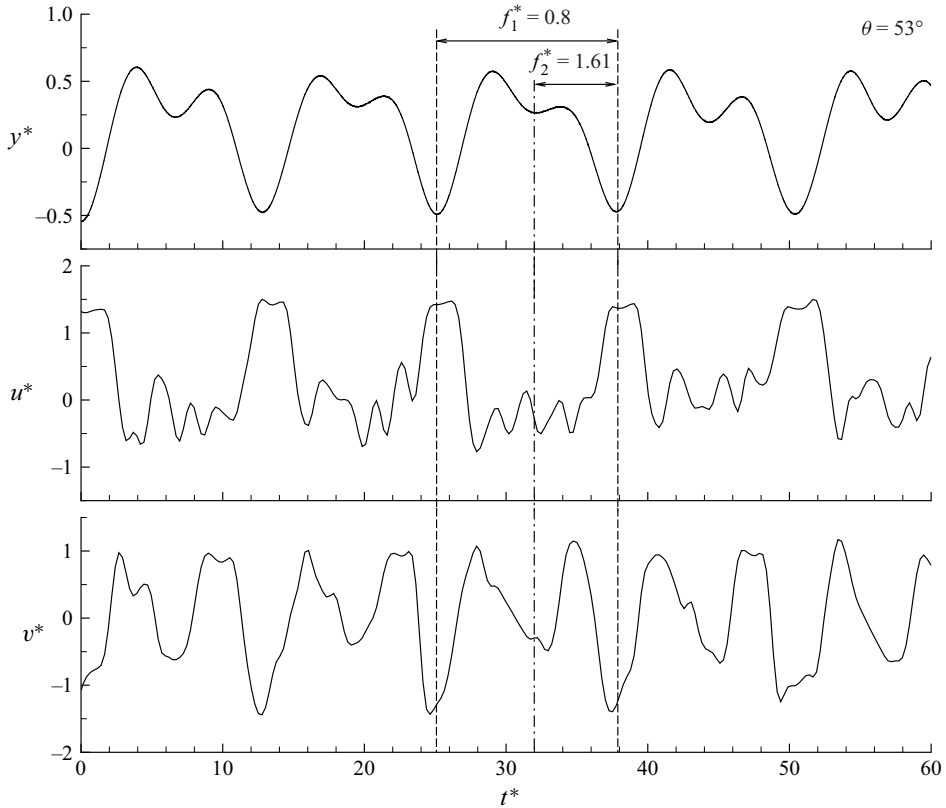


Figure 23. Time traces of displacement of the cylinder  $y^*$ , the streamwise velocity component  $u^*$  and the transverse velocity component  $v^*$  for the wire angular location of  $\theta = 53^\circ$  (from range III). The period of the non-dimensionalized time is the same for all plots. One cycle of oscillation motion is marked between the two vertical dashed lines.

flow fluctuations and the displacement of the cylinder, so the vertical dashed lines show the same values in figures 7(c), 22(a) and 22(b).

To further address the observed double frequency phenomenon in range III, the time traces of cylinder displacement,  $y^*$ , the streamwise velocity component,  $u^*$ , and the transverse velocity component,  $v^*$ , are provided in figure 23 for  $\theta = 53^\circ$  as a representative sample case from the angular range III. The values on the time axis are the same for all plots, and they are presented in non-dimensional form  $t^*$ . The velocity signals are extracted from the PIV data at the point that gives the highest spectral magnitude in the near wake, and the spectra given in figure 22 for  $\theta = 53^\circ$  correspond to the velocity signals shown in figure 23. The vertical dashed lines in figure 23 indicate one full oscillation cycle of the cylinder, and the dash-dot line represents the start of the second reciprocating motion of the cylinder within the cycle. It was mentioned earlier that the oscillation motion in range III is the superposition of two sinusoids with different frequencies. A careful inspection of the displacement signal  $y^*$  reveals that the first dominant frequency  $f_1^*$  (the low value) represents one full cycle of the oscillation motion, and the second dominant frequency  $f_2^*$  (the high value) represents the additional reciprocating motion within the cycle. The two dominant frequencies ( $f_1^*$  and  $f_2^*$ ) are marked in figure 23 for  $\theta = 53^\circ$ . From the time trace of velocity signals in the same figure, it can be observed that the low- and high-frequency

values correspond to the frequency of oscillations in the streamwise and transverse velocity components in the wake, respectively. This observation aligns with the higher spectral magnitude of  $f_1^*$  seen for  $u^*$  in figure 22(a) and the higher spectral magnitude of  $f_2^*$  seen for  $v^*$  in figure 22(b). It should be recalled that four vortices are shed per cycle for the angular range III, as discussed in figure 13. Combined with this knowledge, it can be deduced that the first dominant frequency  $f_1^*$  represents the frequency of the entire vortex shedding process during one oscillation cycle, and the second dominant frequency  $f_2^*$  can be associated with the frequency of shedding for a pair of vortices.

#### 4. Concluding remarks

For a rigid circular cylinder undergoing transversal VIVs with low mass-damping in the lower synchronization range, the extent to which the use of a single spanwise surface wire alters the vibration and vortex shedding characteristics has been investigated by conducting simultaneous PIV and displacement measurements. Motivated by the VIV-based energy harvesting applications from ocean or river flows, the spanwise ends of the cylinder immersed in a water channel were the free water surface at the top and the free end at the bottom. With a diameter equal to 6.25 % of the cylinder diameter, the wire considered in this study had a scale larger than the boundary layer thickness forming around the cylinder. The wire-fitted cylinder was tested at a Reynolds number of 10 000, considering variations in the surface wire location over the complete 180° angular range. Based on the vibration characteristics of the wire-fitted cylinder, several angular ranges were identified for the wire placement. Pattern, amplitude and frequency of the structural oscillations in connection to the vortex shedding modes have been determined for each of these angular ranges. Highlights from these findings are as follows:

Range I ( $0^\circ \leq \theta < 47^\circ$ ): the wire-fitted cylinder undergoes regular sinusoidal motion. A total of two vortices are shed per oscillation cycle, where the vortex on the smooth side of the cylinder undergoes significant stretching and lateral movement, resulting in a time-averaged net lift force toward the wire side of the cylinder.

Range II ( $47^\circ \leq \theta < 51^\circ$ ): placement of the wire within this range causes the cylinder motion to switch intermittently between sinusoidal and irregular oscillations. The intermittent switch in the cylinder motion is linked to a switch in the vortex shedding process, where regular vortex shedding switches into an irregular vortex shedding mode. This switch in the vortex shedding modes is remarkably similar to the sporadic switch between the irregular and regular shedding modes observed in previous studies on stationary cylinders fitted with a surface wire at the first critical location. However, for the oscillating cylinder, this same effect occurs at slightly higher angular positions. Due to the random appearance of irregular cylinder motion and irregular vortex shedding, a single dominant frequency is not discernible for the cylinder oscillations and vortex shedding within this range.

Range III ( $51^\circ \leq \theta < 60^\circ$ ): the wire in this range induces regular cylinder oscillations consisting of a combination of two sinusoidal motions having different frequencies. As a result, these two frequencies co-dominate the cylinder oscillations. This motion is linked to the vortex shedding process where four vortices are shed alternately per cycle, with the shedding of the third vortex inducing a reciprocal cylinder movement. The two dominant frequencies also co-exist in velocity fluctuations, where the lower frequency represents the frequency of the entire vortex shedding process during one complete oscillation cycle, whereas the higher frequency is linked to the shedding of each vortex pair.

Range IV ( $60^\circ \leq \theta < 70^\circ$ ): the wire at angular locations of this range yields quasi-sinusoidal cylinder oscillations along with the random appearance of irregular

motions, although the same vortex shedding process of range III with four alternate vortices shedding per cycle continued to exist in this range.

Range V ( $70^\circ \leq \theta < 75^\circ$ ): the most striking feature of this range is that the amplitude of the wire-fitted cylinder's oscillations increases more than 94% compared with a clean cylinder (with no wire), with the maximum amplitude increase of 102% occurring when the wire is at  $\theta = 73^\circ$ . When the wire is in this range, the cylinder undergoes high-amplitude and near-sinusoidal oscillations. Four vortices are shed per oscillation cycle, similar to ranges III and IV. However, the formation of the third vortex when the cylinder reaches its farthest position on the wire side does not change the cylinder's direction but instead slows it down compared with a sinusoid.

Range VI ( $75^\circ \leq \theta < 105^\circ$ ): the wire-fitted cylinder's oscillations have a quasi-sinusoidal character, with small-amplitude modulations between cycles. Two alternate vortices were shed per oscillation cycle, similar to range I, where sinusoidal oscillation motion was detected. However, vortices in this range appear more stretched and contain more small-scale structures, presumably being the cause of the observed amplitude modulation.

Range VII ( $105^\circ \leq \theta < 109^\circ$ ): the wire in this range stops the sinusoidal oscillation motion of the cylinder and achieves more than 90% reduction in the vibration amplitude compared with a clean cylinder under the same conditions. The maximum amplitude reduction of 98% occurs when the wire is at  $\theta = 107^\circ$ , where the motion of the cylinder almost completely ceases. This is a remarkable finding for VIV suppression applications. There is no dominant frequency for cylinder motion in this range since the cylinder does not oscillate regularly and undergoes only very small-amplitude vibrations. The wire imposes a random switch in the vortex shedding patterns between two modes, named Mode I and Mode II. In Mode I, regular vortex shedding occurs where vortices shed alternately into the wake in a row. On the other hand, in Mode II, vortices form simultaneously on both sides of the cylinder wake, being symmetric about the cylinder centreline. After circulating in their position for a while, these vortices break up into small-scale vortices and then shed downstream.

Range VIII ( $109^\circ \leq \theta \leq 180^\circ$ ): the wire-fitted cylinder returns to its regular sinusoidal motion with one dominant frequency. Four vortices are shed per oscillation cycle of the cylinder, where two vortices of the same sign shed one after the other similar to the 2P vortex shedding mode of clean cylinders oscillating within the lower synchronization range.

One of the prominent results of the present study is that it reveals the existence of two angular ranges that may be significant in practical applications. Enhancing the amplitude of structural oscillations by more than 94% compared with a clean cylinder, with a maximum of 102%, using a wire at range V implies an increase in the extracted energy in VIV-based energy harvesters. On the other hand, more than 90% reduction in VIV amplitude, with a maximum decrease of 98%, using a wire in range VII provides a method to reduce unwanted structural vibrations. Finally, it should be noted that the enhancement and attenuation of the VIV amplitude by placing the wire in angular ranges V and VII, respectively, have also been confirmed to exist for varying reduced velocities in the lower branch (not presented here, but results can be found in Vaziri 2021). However, further investigations should be conducted to evaluate the effect of reduced velocity on the identified angular ranges.

**Acknowledgements.** The authors are pleased to acknowledge the support of the Natural Sciences and Engineering Research Council of Canada (NSERC) under the Discovery grant and the Ministry of Research and Innovation under the Early Researcher Award.

**Declaration of interests.** The authors report no conflict of interest.

**Author ORCIDs.**

-  E. Vaziri <http://orcid.org/0000-0003-1989-4094>;  
 A. Ekmecki <http://orcid.org/0000-0002-5761-7314>.

REFERENCES

- ALAM, M.M., ZHOU, Y., ZHAO, J.M., FLAMAND, O. & BOUJARD, O. 2010 Classification of the tripped cylinder wake and bi-stable phenomenon. *Intl J. Heat Fluid Flow* **31**, 545–560.
- ASSI, G.R.S., BEARMAN, P.W. & KITNEY, N. 2009 Low drag solutions for suppressing vortex-induced vibration of circular cylinders. *J. Fluids Struct.* **25**, 666–675.
- AYDIN, T.B., JOSHI, A. & EKMEKCI, A. 2014 Critical effects of a spanwise surface wire on flow past a circular cylinder and the significance of the wire size and Reynolds number. *J. Fluids Struct.* **51**, 132–147.
- AYDIN, T.B. & EKMEKCI, A. 2014 A robust method to estimate the variation of the vortex shedding frequency with the location of a single spanwise tripwire for circular cylinders in subcritical flow. *J. Wind Eng. Ind. Aerodyn.* **134**, 1–9.
- AZADEH-RANJBAR, V., ELVIN, N. & ANDREOPOULOS, Y. 2018 Vortex-induced vibration of finite-length circular cylinders with spanwise free-ends: Broadening the lock-in envelope. *Phys. Fluids* **30**, 105104.
- BRIKA, D. & LANEVILLE, A. 1993 Vortex-induced vibrations of a long flexible circular cylinder. *J. Fluid Mech.* **250**, 481–508.
- CANPOLAT, C. & SAHIN, B. 2017 Influence of single rectangular groove on the flow past a circular cylinder. *Intl J. Heat Fluid Flow* **64**, 79–88.
- CASTRO HEBRERO, F., *et al.* 2020 Vortex induced vibrations suppression for a cylinder with plasma actuators. *J. Sound Vib.* **468**, 115121.
- CHANG, C.-C. (JIM), AJITH KUMAR, R. & BERNITSAS, M.M. 2011 VIV and galloping of single circular cylinder with surface roughness at  $3.0 \times 10^4 \leq Re \leq 1.2 \times 10^5$ . *Ocean Engng* **38**, 1713–1732.
- CHAPLIN, J.R. & TEIGEN, P. 2003 Steady flow past a vertical surface-piercing circular cylinder. *J. Fluids Struct.* **18**, 271–285.
- EKMEKCI, A. 2006 Control of the near wake of a circular cylinder: effects of surface disturbances. PhD thesis, Lehigh University, Pennsylvania, USA.
- EKMEKCI, A. & ROCKWELL, D. 2010 Effects of a geometrical surface disturbance on flow past a circular cylinder: a large-scale spanwise wire. *J. Fluid Mech.* **665**, 120–157.
- EKMEKCI, A. & ROCKWELL, D. 2011 Control of flow past a circular cylinder via a spanwise surface wire: effect of the wire scale. *Exp. Fluids* **51**, 753–769.
- ERTURK, A. & INMAN, D.J. 2011 *Piezoelectric Energy Harvesting*. John Wiley & Son.
- FENG, C.C. 1968 The measurement of vortex-induced effects in flow past stationary and oscillating circular and D-section cylinders. Master's thesis, University of British Columbia, Vancouver, BC, Canada.
- GABBAI, R.D. & BENAROYA, H. 2005 An overview of modeling and experiments of vortex-induced vibration of circular cylinders. *J. Sound Vib.* **282**, 575–616.
- GONÇALVES, R.T., ROSETTI, G.F., FRANZINI, G.R., MENEGHINI, J.R. & FUJARRA, A.L.C. 2013 Two-degree-of-freedom vortex-induced vibration of circular cylinders with very low aspect ratio and small mass ratio. *J. Fluids Struct.* **39**, 237–257.
- GOVARDHAN, R. & WILLIAMSON, C.H.K. 2000 Modes of vortex formation and frequency response of a freely vibrating cylinder. *J. Fluid Mech.* **420**, 85–130.
- HAY, A.D. 1947 Flow about semi-submerged cylinders of Finite Length. Princeton University Report, Princeton, New Jersey, US.
- HOVER, F.S., TVEDT, H. & TRIANTAFYLLOU, M.S. 2001 Vortex-induced vibrations of a cylinder with tripping wires. *J. Fluid Mech.* **448**, 175–195.
- JOSHI, A. & EKMEKCI, A. 2019 Correlation between single-wire and multi-wire tripping of the flow past a circular cylinder. *Fluid Dyn. Res* **51**, 055506.
- KHALAK, A. & WILLIAMSON, C.H.K. 1997a Investigation of relative effects of mass and damping in vortex-induced vibration of a circular cylinder. *J. Wind Engng Ind. Aerodyn.* **69–71**, 341–350.
- KHALAK, A. & WILLIAMSON, C.H.K. 1997b Fluid forces and dynamics of a hydroelastic structure with very low mass and damping. *J. Fluids Struct.* **11**, 973–982.
- KHASHEHCHI, M., *et al.* 2014 A comparison between the wake behind finned and foamed circular cylinders in cross-flow. *Exp. Therm. Fluid Sci.* **52**, 328–338.
- KHOURY, E. 2012 The influence of end conditions on vortex shedding from a circular cylinder in sub-critical flow. Master's thesis, University of Toronto, Ontario, Canada.

- KONSTANTINIDIS, E. 2014 On the response and wake modes of a cylinder undergoing streamwise vortex-induced vibration. *J. Fluids Struct.* **45**, 256–262.
- LEVY, B. & LIU, Y. 2013 The effects of cactus inspired spines on the aerodynamics of a cylinder. *J. Fluids Struct.* **39**, 335–346.
- MORSE, T.L., GOVARDHAN, R.N. & WILLIAMSON, C.H.K. 2008 The effect of end conditions on the vortex-induced vibration of cylinders. *J. Fluids Struct.* **24**, 1227–1239.
- MORSE, T.L. & WILLIAMSON, C.H.K. 2009 Prediction of vortex-induced vibration response by employing controlled motion. *J. Fluid Mech.* **634**, 5–39.
- NAKAMURA, T. & KANEKO, S. 2008 *Flow Induced Vibrations: Classifications and Lessons from Practical Experiences*. Elsevier.
- NAUDASCHER, E. & ROCKWELL, D. 2012 *Flow-induced Vibrations: An Engineering Guide*. Courier Dover Publications.
- NEBRES, J. & BATILL, S. 1993 Flow about a circular cylinder with a single large-scale surface perturbation. *Exp. Fluids* **15**, 369–379.
- OWEN, J.C., BEARMAN, P.W. & SZEWCZYK, A.A. 2001 Passive control of VIV with drag reduction. *J. Fluids Struct.* **15**, 597–605.
- PRICE, P. 1956 Suppression of the Fluid-Induced Vibration of Circular Cylinders. *J. Engng Mech. Div.* **82**, 1–22.
- QUADRANTE, L.A.R. & NISHI, Y. 2014 Amplification/suppression of flow-induced motions of an elastically mounted circular cylinder by attaching tripping wires. *J. Fluids Struct.* **48**, 93–102.
- SARPKAYA, T. 2004 A critical review of the intrinsic nature of vortex-induced vibrations. *J. Fluids Struct.* **19**, 389–447.
- STANSBY, P.K. 1974 The effects of end plates on the base pressure coefficient of a circular cylinder. *Aeronaut. J.* **78**, 36–37.
- SZEPESY, S. & BEARMAN, P.W. 1992 Aspect ratio and end plate effects on vortex shedding from a circular cylinder. *J. Fluid Mech.* **234**, 191–217.
- ÜNAL, U.O. & ATLAR, M. 2010 An experimental investigation into the effect of vortex generators on the near-wake flow of a circular cylinder. *Exp. Fluids* **48**, 1059–1079.
- VAZIRI, E. 2021 Vortex-induced vibration and forced oscillation motion of a circular cylinder fitted with a single spanwise tripwire. PhD thesis, University of Toronto, Ontario, Canada.
- VINOD, A., AUVIL, A. & BANERJEE, A. 2018 On passive control of transition to galloping of a circular cylinder undergoing vortex induced vibration using thick strips. *Ocean Engng* **163**, 223–231.
- WILLIAMSON, C.H.K. & GOVARDHAN, R. 2004 Vortex-Induced Vibrations. *Annu. Rev. Fluid Mech.* **36**, 413–455.
- WILLIAMSON, C.H.K. & GOVARDHAN, R. 2008 A brief review of recent results in vortex-induced vibrations. *J. Wind Engng Ind. Aerodyn.* **96**, 713–735.
- WILLIAMSON, C.H.K. & ROSHKO, A. 1988 Vortex formation in the wake of an oscillating cylinder. *J. Fluids Struct.* **2**, 355–381.
- ZHOU, B., *et al.* 2015 Experimental study on flow past a circular cylinder with rough surface. *Ocean Engng* **109**, 7–13.
- ZHOU, T., *et al.* 2011 On the study of vortex-induced vibration of a cylinder with helical strakes. *J. Fluids Struct.* **27**, 903–917.